Journal of Materials Chemistry A

The Coupling of Experiments with Density Functional Theory in the Studies of Electrochemical Hydrogen Evolution Reaction

Journal:	*Journal of Materials Chemistry A*
Manuscript ID	TA-REV-03-2020-002549.R1
Article Type:	Review Article
Date Submitted by the Author:	12-Apr-2020
Complete List of Authors:	Chen, Mingpeng; University of California, Department of Chemistry and Biochemistry Smart, Tyler; University of California, Department of Physics Wang, Shanwen; University of California, Department of Chemistry and Biochemistry Kou, Tianyi; University of California, Santa Cruz, Chemistry and Biochemistry Lin, Dun; University of California, Department of Chemistry and Biochemistry Ping, Yuan; University of California Santa Cruz, Chemistry and Biochemistry Li, Yat; University of California, Department of Chemistry and Biochemistry

The Coupling of Experiments with Density Functional Theory in the Studies of Electrochemical Hydrogen Evolution Reaction

Mingpeng Chen[1], Tyler J. Smart[2], Shanwen Wang[1], Tianyi Kou[1], Dun Lin[1], Yuan Ping[1*], Yat Li[1*]

[1]Department of Chemistry and Biochemistry, University of California Santa Cruz, 1156 High Street, Santa Cruz, California, 95064, USA

[2]Department of Physics, University of California Santa Cruz, 1156 High Street, Santa Cruz, California, 95064, USA

Corresponding authors: yuanping@ucsc.edu; yatli@ucsc.edu

Abstract

Hydrogen evolution reaction (HER) is the cathodic reaction of water electrolysis, which is a cleaner and more sustainable approach to produce hydrogen gas compared to the conventional steam reforming method. Electrocatalysts are essential to lower the overpotential of HER and, thus, the overall energy cost of water electrolysis. The search of high performance HER catalysts has been facilitated by coupling experiments with first principles calculation, *e.g.,* density functional theory (DFT). This article will first review the factors determining the performance of HER electrocatalysts. Then, we will discuss the power of coupling experiments with DFT in obtaining insights into the fundamentals of HER, including explaining experimental results and revealing reaction mechanisms, and facilitating the development of new HER electrocatalysts. The last section of this review focuses on the limitations and progress of coupling experiments with DFT from three perspectives: experimental measurements, characterization and DFT simulation. Finally, we share some opinions about how to better couple experiments with DFT.

1. Introduction

Hydrogen gas is one of the most important chemicals, which has been widely used for petroleum refining,[1, 2] ammonia production,[3, 4] fuel cell,[5, 6] *etc*. The demand for hydrogen increases exponentially with the increasing global population. To date, steam reforming of natural gas is still the most commonly used industrial method to produce hydrogen gas.[7] However, the process not only uses non-renewable energy sources but also produces a large amount of carbon dioxide. Water electrolysis is an alternative and more sustainable approach to produce hydrogen gas. If water electrolysis is powered by renewable energy sources such as solar energy, wind energy, *etc*., then the carbon footprint for hydrogen generation can be further reduced. Hydrogen evolution reaction (HER) is the cathodic reaction of water electrolysis. A highly efficient HER electrocatalyst is essential to decrease the overpotential of HER and, thus, the overall energy cost of water electrolysis. Platinum (Pt) is known to be the most efficient electrocatalyst for HER.[8] However, the scarcity and high cost of Pt limit its large scale applications. Replacing platinum with earth-abundant, inexpensive and highly efficient electrocatalysts has been an outstanding challenge in the field. Fortunately, the searching of such electrocatalysts can be facilitated by coupling experiments with first principles calculations, *e.g.* density functional theory (DFT).[9]

DFT has become a popular method to investigate the properties of molecular and solid-state materials because of the following reasons: (1) it is able to deal with many-body problems with a relatively economical computational cost compared to other high-cost theories such as random-phase approximation, Møller–Plesset perturbation theory, coupled-cluster singles and doubles method, quantum Monte Carlo calculation, *etc*. (2) Its accuracy has been improved significantly in the past several decades by using better functionals to a level that is sufficient to explain or predict the properties of interested materials.[10-15] (3) As shown in Figure 1, the

computation capability worldwide in the past 30 years has an exponential increase, which makes it possible to use DFT to calculate larger and more complicated systems.[16-19]

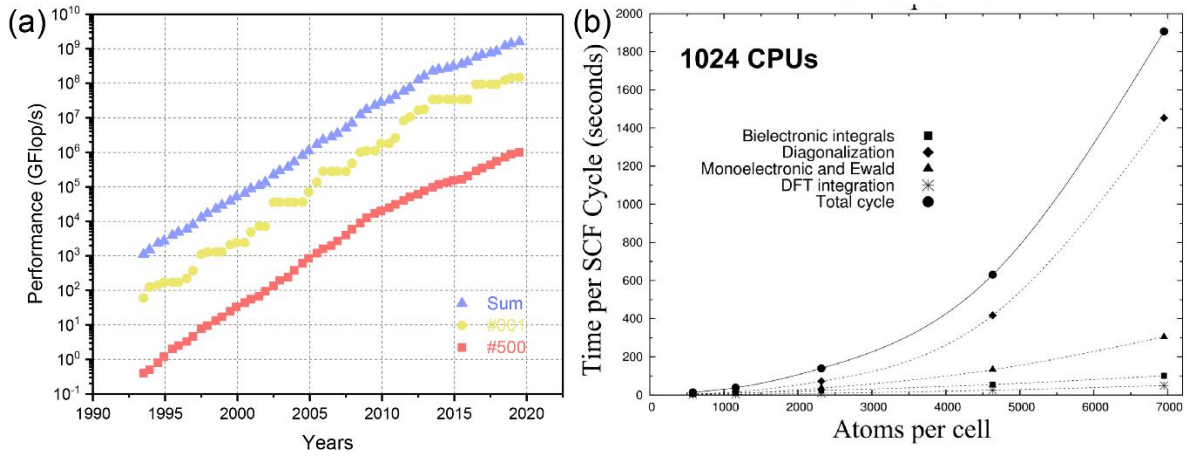

Figure 1. Computation capability development and computation time scale with the number of atoms per cell. (a) The y-axis (Flop/s) in (a) means floating point operations per second, which is a metric to evaluate the computer performance.[16] "#001" means the fastest supercomputer in the world, "#500" means the 500th fastest supercomputer in the world and "Sum" means the summation computation capability of the top 500 supercomputers. (b) Wall-clock time (in seconds) of a SCF cycle run in parallel over 1024 processors for MCM-41 supercells of increasing size with the hybrid B3LYP functional. The time required by the main computational tasks at each SCF cycle is also separately reported. Figure (a) reproduced from Ref.16, copyright 2019, with permission from TOP 500 website, (b) reprinted from Ref.18, copyright 2017, with permission from American Chemical Society.

In this review, we will focus on the accomplishments and challenges of the coupling between experiments and DFT. We will start with the discussion on important factors for determining the performance of HER electrocatalyst. The first factor is the thermodynamic adsorption of intermediate H. There are many pathways to manipulate this factor, strategies of heteroatom doping, vacancy engineering and strain engineering are discussed in the review.[20-22] The kinetics of H_2O dissociation are the second factor, and strategies of orbital engineering and

heterogeneous interface construction are discussed.[23, 24] The third one is the thermodynamic adsorption of OH^-, which plays an important role in refreshing the active sites and tuning the energy barrier of H_2O dissociation.[25] Conductivity of electrode and the charge transfer between electrode and electrolyte are two other factors, and they are often coupled with each other and it's usually difficult to distinguish their individual contribution.[26, 27] The former consists of three parts: the conductivity of substrate and catalyst, as well as the electric contact between them, while the latter is governed by a lot of factors such as potential, surface area, conductivity of electrode/electrolyte, *etc*. Besides, bubble effect cannot be neglected and it becomes significant at large current. Two methods for facilitating the detachment of bubbles, creating nanostructures and making electrode surface superaerophobic, are discussed in this review.[28, 29] Last but not least, we review the stability of electrocatalyst, in which different degradation mechanisms are discussed.[30, 31] Suggestions on how to improve the stability of electrocatalyst are also provided.

The second section focuses on the accomplishments by coupling experiments with DFT, which are summarized from two perspectives. First, it helps to gain insights into the fundamentals of HER, including explaining anomalous experimental phenomena such as the pH dependence of H binding energy on a metal surface,[32] and predicting reaction mechanisms of HER on different surfaces,[33-35] which are still hard to be studied experimentally. Second, it facilitates the development of new HER electrocatalysts such as transition metal dichalcogenides (TMD), carbon-based materials, single-atom catalysts (SACs) and MXene.[36-39] For instance, the study of MoS_2 is the earliest demonstration of how DFT helps the search of promising HER electrocatalyst by using the Gibbs free energy of hydrogen adsorption as the descriptor.[36] Since then, a series of other TMD were also found to have similar attractive Gibbs free energy of hydrogen adsorption values as MoS_2, which expanded the scope from one material to one class of materials. Although

pristine MoS_2 shows a decent HER activity, it is still not comparable to that of Pt. The reasons include the poor conductivity, low density of active edge sites and low activity of largely exposed basal planes of 2H phase MoS_2. The corresponding strategies of utilizing 1T metallic phase MoS_2, maximizing the number of edge sites and activating the inert basal planes of 2H phase MoS_2 were developed to further boost the activity of MoS_2, trying to make it comparable to that of Pt.[40-42] DFT also contributed to the development of carbon-based HER catalysts. Carbon-based materials are attractive because of their low cost, high abundance, and high corrosion resistance. However, the pristine carbon-based material is known to be inert for catalyzing HER. Different approaches have been employed to engineer carbon-based materials' electronic structures and increase their activities. Among them, doping was found to be one of the most effective methods.[37] Although many heteroatoms (*e.g.*, B, N, O, P, S) have been demonstrated to be useful in boosting the HER activity of carbon, it is still challenging to understand the possible synergistic effect between dopants. DFT calculation can serve as an efficient tool to gain more insights about the interaction between different dopants. SACs are another emerging type of material for catalyzing HER. Different from metal bulk or nanostructures, where metal atoms stack with each other and form crystal structures, single metal atoms in SACs are distributed and confined in the substrate such as carbon-based materials or transition metal oxides. People are interesting in SACs because it can achieve the 100% utilization of metallic atoms and minimize metal loading, which is important for practical application, especially for noble metal-based catalysts. For SACs, a challenge is to find suitable dopants for a specific substrate. DFT can help to simplify and accelerate this searching process. Instead of testing different dopants experimentally, DFT screening is a more efficient and cheaper method to search for the correct dopants for a specific substrate.[43] MXene, a new class of two-dimensional material, were also reported to show promising HER performance recently.[39]

DFT calculation systematically studied a series of MXene and found that they are all conductive under standard conditions and can own a favorable H adsorption activity when the surface is terminated with suitable groups.[44] These computational works motivated and guided more experimental efforts on MXene.

There are also a number of unaddressed issues and challenges for coupling experiments with DFT. We discuss these challenges from three perspectives: experimental measurements, characterization and DFT simulation. In the subsection of experimental measurements, the significance of scan rates, reactants diffusion, bubble management, and intrinsic activity comparison is highlighted. The determination of an accurate ECSA is important for comparing the intrinsic activity of different catalysts. Different methods for measuring the ECSA are summarized and compared.[45] Characterization provides critical structural information to build models for DFT calculation. The characterization subsection presents the recent advancement of *in-situ/operando* techniques, and discusses some new discoveries made by using these techniques. For example, Deng *et al.* employed operando Raman spectroscopy to study amorphous MoS_x for HER and proved that S sites are the active HER sites.[46] From the perspective of DFT simulation, there are two major challenges. One is the fundamental limitation of DFT methodology, while the other is the simulation of the interface between the electrolyte and electrified electrode. Although DFT achieves a good balance between computation costs and accuracy, this method has issues of inaccurate electron correlation, zero temperature calculation, entropy approximation, *etc*. The issue of inaccurate electron correlation is more obvious when it comes to strongly correlated systems such as many transition metal oxides.[47] For the simulation of the interface between the electrolyte and electrified electrode, we discuss the discrepancy between the current computation environment and the real working environment, including (1) potential, (2) solvent, (3) solute and

(4) pH. The widely used constant charge scheme cannot correctly simulate the effect of potential on the reaction pathway since potential only affects the energy of electrochemical steps in this scheme.[48] On the contrary, the constant potential scheme is able to capture the effect of potential on non-electrochemical steps correctly. For example, Ping *et al.* employed the constant potential scheme to study the reaction mechanism of oxygen evolution reaction (OER) on IrO_2, and showed that the non-electrochemical steps at the constant charge condition can be strongly electrochemical dependent at the realistic constant potential condition.[49] There are two general approaches to include the effect of solvent, explicit solvent models and implicit solvent models. Although explicit solvent models give more insights about the interaction between solvents and solutes,[32, 50-52] it's more computational expensive. Implicit solvent models, on the other hand, replace explicit solvent molecules with a polarizable dielectric media, in which case is relatively more computational economical and can provide an average description of the overall solvent behavior. There are some new implicit solvent models developed recently such as the charge-asymmetric nonlocally determined local-electric (CANDLE) solvent model, which enables an explicit treatment of the charge asymmetric solvents.[53] The effect of solutes also has to be taken into account, and it has been demonstrated by Pham *et al.* that it can be quantitatively described by using first principles molecular dynamics (MD) calculations and electronic structure calculations with dielectric dependent hybrid functionals.[54] pH effect is complicated, however, important to be included in the computation environment. One easy approach to simulate pH effect is to convert the pH effect to potential effect by using the Nernst equation, but it cannot fully describe the pH effect.[32] The pH effect can also be depicted by correlating the pH to the chemical potential of isolated ions. Ambrosio *et al.* employed this method to study the pH dependence on $BiVO_4$ (010) surface and found that protons, H_2O molecules, and hydroxyl groups are the dominant groups in the strong

acidic media, media with pH ranging from 2 to 8 and pH larger than 8.2, respectively.[55] In the last section, we also proposed some strategies to improve the coupling between experiments and DFT calculations.

2. The key factors for determining the performance of HER electrocatalysts

A number of important factors (Figure 2) that determine the performance of HER electrocatalysts are discussed in this section. The discussion of each factor starts with a general background, followed by representative examples to illustrate how this factor affects the performance of HER electrocatalysts. Improving the overpotential of HER electrocatalysts is one of the most important goals in the community. Unfortunately, there is no simple answer for the question of how to improve the HER overpotential down to the level of Pt. Different materials have different intrinsic catalytic activities for each step in HER, so a distinct approach is needed for each catalyst. Despite the complexity of the question, there are some general approaches to improve the activity of HER electrocatalyst such as improving the conductivity, increasing the number of active sites and enhancing the intrinsic activity of each active site. For example, MoS_2 is a representative HER material.[36] Its activity is known to be hindered by the poor conductivity. Therefore, using 1T metallic phase MoS_2 can increase its activity.[40] Jaramillo *et al.* found that the edges of 2H semiconducting phase MoS_2 are active sites,[42] so structural engineering approach has been employed to maximize the number of exposed edge sites.[56, 57] In addition, vacancy and strain engineering have also been employed to activate the inert 2H MoS_2 basal plane.[41] Orbital engineering approach has been used to improve the activity of MoS_2 in alkaline medium.[58] For other materials, for example, pristine carbon-based materials are known to be inert for catalyzing HER. Strategies such as heteroatom doping have been taken to boost its activity. 3-dimensional

graphene structures achieved a current density of 10 mA cm^{-2} at a small overpotential of 107 mV.[59] Transition metal oxides such as NiO, are known to be good materials for H_2O adsorption and dissociation but lack active H adsorption sites. By creating more favorable H adsorption sites on the surface via doping, its activity has been significantly improved to close to the level of Pt, with an ultrasmall overpotential of 27 eV at a current density of 10 mA cm^{-2}.[60] These examples suggest that specific strategies are required to tackle specific limitations in different HER materials. A general approach is to first understand the catalytic mechanism of the HER catalyst, identify the questions needed to be addressed, and then develop the right strategies through the combination of computational and experimental efforts.

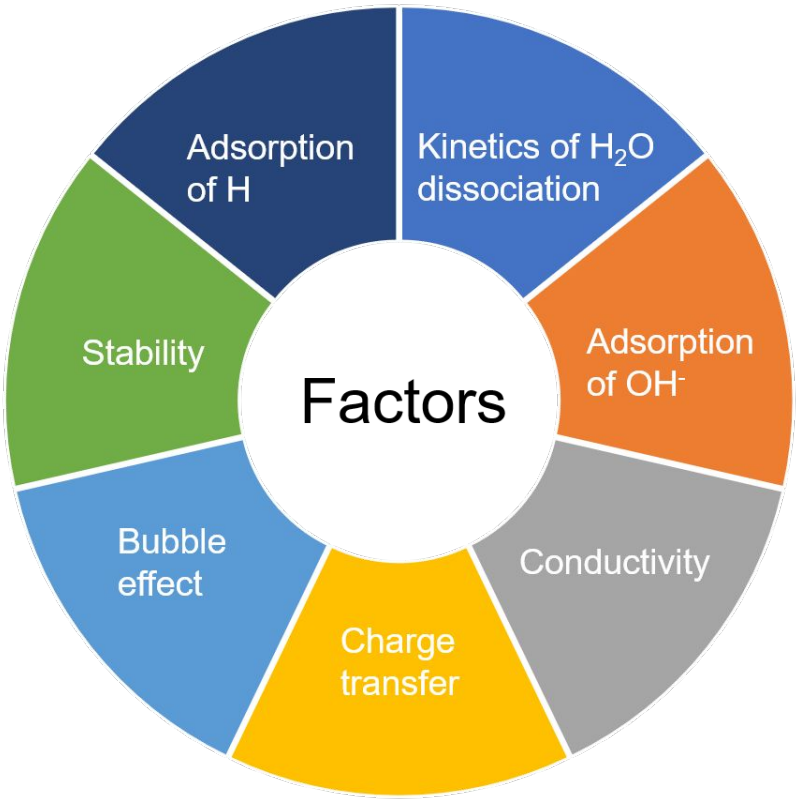

Figure 2. Important factors that determine the performance of HER electrocatalysts.

2.1. Thermodynamic adsorption of intermediate H

HER consists of two steps.[61] The first step is called the Volmer step, in which intermediate H is generated. For the second step, there are two possible mechanistic pathways: Heyrovsky step and Tafel step. In the Heyrovsky step, intermediate H reacts with another proton or H_2O molecule to generate an H_2 molecule. Alternatively, two intermediate H combine to form H_2 molecule in the Tafel step.[62, 63] Depending on the reaction media, the reaction mechanism would be different. In an acidic media, the reactions are:

Volmer step: $* + H^+ + e^- \rightarrow *H$ (1)

Heyrovsky step: $*H + H^+ + e^- \rightarrow *H_2$ (2)

Tafel step: $*H + *H \rightarrow *H_2$ (3)

Among which, $*$ is the active site on the surface. In alkaline media, an additional H_2O dissociation step is required to generate intermediate H,[64] then the reactions are:

Volmer step: $* + H_2O + e^- \rightarrow *H + OH^-$ (4)

Heyrovsky step: $*H + H_2O + e^- \rightarrow *H_2 + OH^-$ (5)

Tafel step: $*H + *H \rightarrow *H_2$ (6)

Previous studies showed that the activity of HER electrocatalysts is closely related to the thermodynamic adsorption of intermediate H on the surface of electrocatalyst, whose strength can be evaluated by the Gibbs free energy of H adsorption (ΔG_H^*).[36] The widely accepted equation for calculating the ΔG_H^* is:[36, 49]

$$\Delta G_H^* = \Delta E_H^* - T\Delta S + \Delta ZPE + \Delta E_{solvation} \quad (7)$$

Among which, the ΔE_H^* is the enthalpy difference between surface with and without hydrogen, $T\Delta S$ is the entropy contribution, ΔZPE is the change of zero-point energy while $\Delta E_{solvation}$ is the change of solvation energy contribution. There are different methods to calculate solvation energy. Each method has its own pros and cons, which will be discussed in section 4.3.2.2. If ΔG_H^* is much smaller than 0, it means that the adsorption of H on the surface is too strong, which is hard for H to desorb from the surface and would lead to a high energy barrier for the Heyrovsky/Tafel step. On the other hand, a very positive ΔG_H^* would cause a high energy barrier for the Volmer step. A value of ΔG_H^* close to 0 represents the optimal thermodynamic adsorption for hydrogen. This relationship proposed by Nørskov *et al.* is called the "Volcano plot".[65] The y-axis of the "Volcano plot" is the exchange current density (j_0), an experimental parameter to evaluate the intrinsic activity of the electrocatalyst. The larger the j_0, the higher the intrinsic activity. While tuning the value of ΔG_H^* has been proved to be an effective approach to enhance the activity of some HER catalysts, it is necessary to point out that a ΔG_H^* close to 0 does not guarantee a high HER activity, which depends on other parameters as well.[36] Some commonly used approaches for tuning the value of ΔG_H^* of HER electrocatalysts are discussed in the following part.

2.1.1. Heteroatom doping

Doping is one of the most widely used approaches to tune the physical and chemical properties of pristine materials and found to be effective in manipulating ΔG_H^* via redistributing charge, creating dangling bonds, changing the coordination numbers, *etc*.[20, 66] For examples, $NiCo_2S_4$ is an active HER electrocatalyst because of its high conductivity and the presence of

hybrid d orbitals between Ni and Co.[58] However, its activity was hindered by the strong interaction between H and S sites, which slows down the kinetics of H desorption from these sites.[67, 68] Wu *et al.* successfully modulated the electron density of $NiCo_2S_4$ and facilitated the desorption of H from those S sites via the incorporation of N dopants.[58] Due to the strong electronegativity of N, the electron density of S decreases after N doping, which makes the desorption of H from these S sites easier. The concept of N doping was also tested for other metal sulfides, including FeS_2, NiS_2, and CoS_2. All of them showed an obvious performance improvement, suggesting it is a general approach to tune the electron density of S sites in metal sulfides. Ni_3S_2 is also a promising HER electrocatalyst because of its metallic property that can facilitate the interfacial charge transfer. However, the adsorption of H on S sites is also not favorable and limits the performance of Ni_3S_2. Recently, Kou *et al.* demonstrated the incorporation of N into Ni_3S_2 can address this issue.[69] DFT calculation found that the coordination number of S decreased after N doping and more dangling bonds were exposed, which facilitated the adsorption of H. In addition, the incorporated N dopants can serve as new active H adsorption sites, depending on the coordination number of N. If the coordination number of N is low (*e.g.*, 3), then too many exposed dangling bonds coupled with the strong electronegativity of N makes the adsorption of H on N sites too strong. On the contrary, if the coordination number of N is high (*e.g.*, 5), the less dangling bonds combined with the strong electronegativity of N creates a favorable ΔG_H^* on N sites. The role of N is to tune the coordination number of S and serve as potential active H adsorption sites. NiO is another well studied HER electrocatalyst since it is favorable for the adsorption and dissociation of H_2O molecules. However, the overall performance of pristine NiO is limited by its unfavorable H adsorption activity. Kou *et al.* tackled this issue by doping carbon into NiO to switch the H adsorption activity of NiO.[60] The carbon doped NiO achieved an ultralow overpotential of 27 mV at the current density of 10 mA

cm^{-2}. DFT calculation found that the carbon dopant distorted the local structure of NiO and decreased the coordination number of outermost layer Ni sites from 3 to 2, which enriched the electron density on these Ni sites as evidenced by the consistent agreement between projected density of states (PDOS), electron density mapping and atomic charge difference (ΔQ) analysis, as shown in Figure 3. The analysis further revealed that the shift of ΔG_H^* is associated with two factors, the number of Ni sites that H bind to and the ΔQ of Ni. If the structure has similar ΔQ, then the more Ni that H bind to give a ΔG_H^* closer to 0, which is due to the stronger interaction between H and multi-fold Ni. On the other hand, if H bind to the same number of Ni sites, then a larger ΔQ gives a ΔG_H^* closer to 0, because the higher electron density of Ni makes it easier for H to bind with. It is anticipated that other *n*-type dopants such as Si, N and P with smaller atomic size than Ni could have a similar effect as carbon dopant in tuning the electron density of Ni sites and H adsorption activity on them.

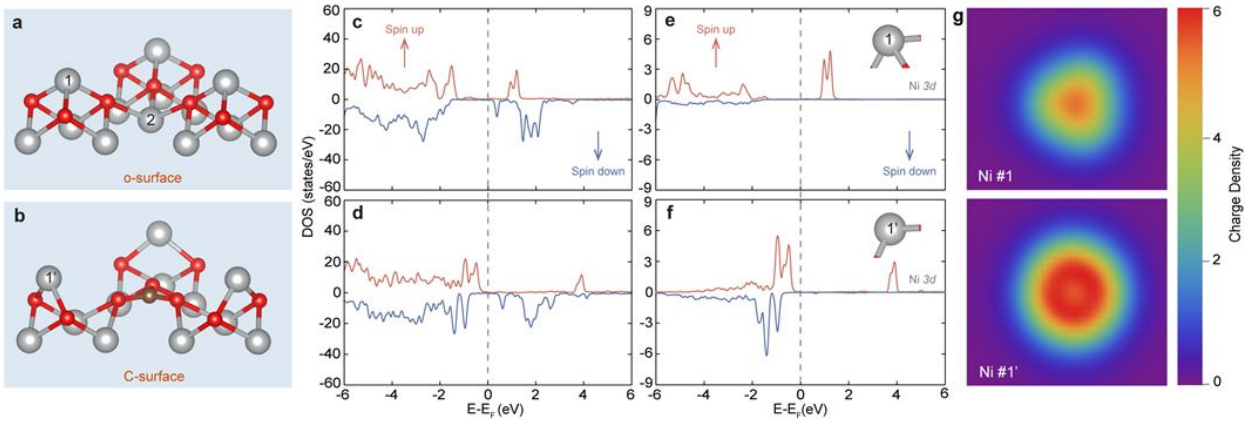

Figure 3. Surface structure, PDOS and electron density mapping in o-surface and C-surface. (a)(b) the structures of o-surface and C-surface. (c)(d) the PDOS of the Ni 3d and O 2p of the first three layers from o-surface and C-surface. (e)(f) the PDOS of the 3d orbitals of Ni on o-surface (Ni #1) and C-surface (Ni #1'), respectively. (g) charge density mapping of the outermost Ni (#1 and 1') on o-surface (upper) and C-surface (bottom). Reprinted from Ref.60, copyright 2020, with permission from Springer.

2.1.2. Vacancy engineering

The thermodynamic adsorption of H strongly depends on the coordination number of active sites. The existence of vacancies on the catalyst surface can create under-coordinated sites, which have more dangling bonds and usually show higher activity than the regular fully coordinated sites.[21] Therefore, vacancy engineering is another effective approach to adjust the thermodynamic adsorption of H. For example, in an early study, Raybaud *et al.* reported that the basal plane of 2H phase MoS_2 is inactive toward the adsorption of H.[70] How to activate the basal plane of 2H phase MoS_2 has been a challenging and interesting topic in the field. Li *et al.* successfully demonstrated how to activate the basal plane of 2H phase MoS_2 through the synergistic effect of strain and S vacancies.[41] The capillary force was first introduced to strain the lattice of MoS_2, and followed by Ar plasma etching to create S vacancies on the surface. The level of strain and the concentration of S vacancies were controlled by adjusting the topography of the gold nanocones and the Ar plasma etching time. DFT calculation showed that the introduction of S vacancies on the surface brings more gaps states near the Fermi level, allowing H to adsorb on the exposed Mo sites easily. On the other hand, the applied tensile strain shifted both the valence band maximum (VBM) and conduction band minimum (CBM) closer to the Fermi level, resulting in a narrower bandgap and more gap states, which also facilitated the adsorption of H. The strain and vacancies engineered basal plane of 2H-MoS_2 showed an even higher activity than the edge-site only MoS_2. Tungsten trioxide (WO_3) is another attractive material for HER because of its high abundance and excellent electrochemical stability for HER. However, its activity is hampered by its poor conductivity and unfavorable H adsorption activity. In order to solve these issues, Zheng *et al.* introduced oxygen vacancies in the structure of WO_3 by liquid exfoliation method.[71] The concentration of oxygen

vacancies was controlled by the annealing time in the air. The authors demonstrated that the enriched oxygen vacancies in the structure introduced more gap states, which simultaneously improves the conductivity and the H adsorption activity of WO_{3-x}.

2.1.3. Strain engineering

Strain engineering is another commonly used method to manipulate the H adsorption activity of catalysts via tuning the DOS of active sites near the Fermi level.[22, 72, 73] For example, Voiry *et al.* systematically studied the role of strain in tuning the ΔG_H^* of WS_2.[74] By chemically exfoliating the lithium intercalated WS_2 powders, the strain was introduced in the exfoliated monolayer WS_2 nanosheet (NS) and observed by using high-angle annular dark-field (HAADF) aberration-corrected scanning transmission electron microscope (STEM). The authors performed DFT calculation and found that by gradually increasing strain from 0 to 4% on metallic 1T phase WS_2, the DOS near the Fermi level increased accordingly. As a result, the value of ΔG_H^* shifted from 0.28 eV to -0.15 eV. Interestingly, the HER activity was not improved when the strain was applied on semiconducting 2H phase WS_2. They also found that only tensile strain can tune ΔG_H^* effectively while compressive strain did not. The combination of experiments and DFT proved that the tensile strain must couple with 1T metallic phase to facilitate the adsorption of H on WS_2.

d band theory can be used to well explain how strain tunes the value of ΔG_H^* for metal systems.[75-77] The principle of d band theory is that the adsorption strength of adsorbates on a surface strongly depends on its surface electronic structure. For example, when oxygen-containing species adsorb on metal, the p orbitals of oxygen interact with the d orbitals of metal to generate bonding orbitals and antibonding orbitals. The formation of bonding orbitals is similar for all metal

surfaces. However, the filling of antibonding orbitals is strongly affected by the d band level of the metal surface. A deeper d-band center would lead to an increased filling of antibonding orbitals and weaken the bonding of adsorbates. The d band center could be manipulated by the introduction of strain. Yan *et al.* systematically studied the effect of strain on different metals (*e.g.*, Ni, Cu, and Pt) towards HER.[78] Since these metals lie in different positions in the "Volcano plot", they have different responses to the strain. For example, the positions of Ni and Pt on the left side of the volcano plot indicate a very strong H adsorption. The application of compressive strain shifts the d band center down. A deeper d band means a larger overlap with the orbitals of H and more antibonding orbitals are filled, which destabilizes the adsorption of H and makes ΔG_H^* closer to 0. In contrast, the H adsorption on Cu is weak, so tensile strain should be applied to upshift the d band center, and consequently stabilize the adsorption of H. Their experimental results are consistent with the DFT calculation results and the d band theory, demonstrating that strain engineering can serve as an effective approach to tune the activity of H adsorption.[75, 76, 78-80] Li *et al.* demonstrated a good example about how to combine strain engineering with other strategies to steer the adsorption/desorption of intermediates.[81] Ag has been considered to be an inactive HER electrocatalyst for decades. One of the reasons is the weak adsorption of H on the surface of Ag. Li *et al.* successfully tackled this issue through laser ablation in liquid method to introduce a high density of stacking faults, which created a low coordination number environment and high tensile strain in the structure. DFT calculation found that the coupling of low coordination number and tensile strain together successfully manipulated the adsorption activity of H on the surface of Ag. The ΔG_H^* of Ag (111) surface shifted from ~ 0.6 eV to optimal thermodynamic value of 0 on a strained Ag surface (Figure 4c and d). Wang *et al.* also used strain engineering to tune the activity of two-dimensional transition metals for HER.[82] Interestingly, they didn't use any heterogeneous

substrate to generate strain, instead, intrinsic strain was introduced and fine-tuned by controlling the thickness of two-dimensional transition metals nanosheets since the cleavage of bulk metal atoms often leads to charge redistribution and attractive interactions between surface atoms. The DFT calculation revealed that the attractive interaction between surface atoms introduces surface tensile strain, and the level of strain is inversely proportional to the thickness of nanosheets. Likewise, the HER activity of Pd nanosheets were also experimentally found to be strongly correlated to the thickness of Pd nanosheets, again proofing the success of strain engineering in tuning the HER performance of metals.

2.2. Kinetics of H_2O dissociation

It's well-known that the activity of Pt in alkaline medium is two to three orders lower than that in acidic media.[83] There are different explanations.[32, 84-89] Although some of them are still controversial, one of the most widely accepted explanations attributes this phenomenon to the pH dependence of energy barrier for the dissociation of H_2O molecule in alkaline medium.[90] Therefore, it is important to consider this factor in evaluating or designing new HER electrocatalysts. According to the Arrhenius equation, the energy barrier can be determined by plotting the reaction rates as a function of temperature.[91] It's highly recommended to use the stable current extracted from the current-time measurements with a dwell time of at least 5 minutes and then use the following equation to convert current density (j) to reaction rates (R):[49]

$$log_{10} j(\eta) = log_{10}(nFN_A^{-1}R(\eta)) \quad (8)$$

It is noteworthy that the energy barrier extracted from this method includes not only the combined energy barriers of the elementary steps (Volmer step and Heyrovsky/Tafel step) of HER but also

the barriers contributed from the mass diffusion of bubbles and reactants. As a result, sometimes it's hard to compare the experimental data with the calculated one, which does not consider the factor of mass transfer. There are two general methods to calculate the energy barrier of H_2O dissociation, *ab initio* molecular dynamics (MD) free energy sampling and static configuration. For the former, one can evaluate the forces using quantum mechanics (*e.g.,* DFT) and move atoms based on classical Newton's equation (often termed as *ab initio MD*). To get the reaction barriers, one needs to use enhanced sampling methods such as meta-dynamics and constrained MD at finite temperature for the catalyst systems with explicit liquid water. Such methods are expensive and have been applied only to limited systems.[50, 51] The latter is a cheaper and more commonly used method, but it requires careful examination of water interaction with the catalyst surface. In this review, we mainly focus on static configuration calculation, and the two most commonly used DFT calculation methods will be reviewed here. The first one is the Nudged Elastic Band (NEB) method, which aims to determine the saddle point and find the minimum reaction pathway between the known reactants and products.[92, 93] A series of intermediates along the reaction pathway will be generated through the linear combination of initial structure and final structure, and every image would be optimized to find the lowest possible energy, which is constrained by a spring force between different images and projecting out the component of the force. Different from the NEB method, which is an interpolation method to find the reaction pathway and transition state, the DIMER method, a local saddle-point search algorithms method via computing either exact or approximate Hessians, can also be used to search for the transition state. DIMER calculation starts from a minimum basin and searches in random directions until it finds the SP. This method is aimed to deal with systems with a complicated reaction pathway in high dimensional configuration

space. Due to the slow convergence of NEB calculation, the DIMER method can be coupled with the NEB method to speed up the calculation and help find the saddle point accurately.[94, 95]

Given the important role of the H_2O dissociation step for HER, several approaches have been reported to improve the kinetics of H_2O dissociation. Two commonly used approaches are discussed in the following part.

2.2.1. Orbital engineering

The dissociation of H_2O molecules on the surface of HER electrocatalyst largely depends on the orbital orientation of active sites. An unfavorable orbital orientation could slow down the kinetics of H_2O dissociation.[23] For example, MoS_2 typically shows a decent HER performance in an acidic medium because of the favorable adsorption of protons.[36] However, its performance is much lower in an alkaline medium because its orbital orientation is not favorable for the adsorption and dissociation of H_2O molecules.[96] Recently Zang *et al.* have successfully solved this problem by doping MoS_2 with carbon.[23] The carbon doped MoS_2 achieved a current density of 10 mA cm^{-2} with an overpotential of only 45 mV, which is the best performance among all ever reported MoS_2 based material in alkaline medium. Their DFT calculation found that the carbon dopant formed an sp^2 hybridization structure in MoS_2 and created an empty 2p orbital. The vertical characteristic of empty 2p orbital facilitates the adsorption and dissociation of H_2O molecules (Figure 4). Their DFT calculation and experimental results consistently proved the role of carbon in manipulating the orbital orientation to facilitate H_2O dissociation. It is anticipated that the lower HER activity of Pt in alkaline medium is also due to the slow kinetics of H_2O dissociation, as a result of the unfavorable orbital orientation. Xie *et al.* demonstrated how to tune the orbital orientation of Pt-Ni nanowires via N doping, which specifically bonded with Ni sites and provided empty d_{z^2} orbital.[97] The surface electrostatic potential mapping analysis revealed the importance

of empty d_{z^2} orbitals for the adsorption and dissociation of H_2O molecule. N doping method was also employed to tackle the unfavorable orbital orientation in Pt-Co and Pt-Cu structures. All these N doped Pt-based alloys showed enhanced HER performance. These previous studies prove that orbital engineering is an effective approach to facilitate the dissociation of H_2O molecules in an alkaline medium.

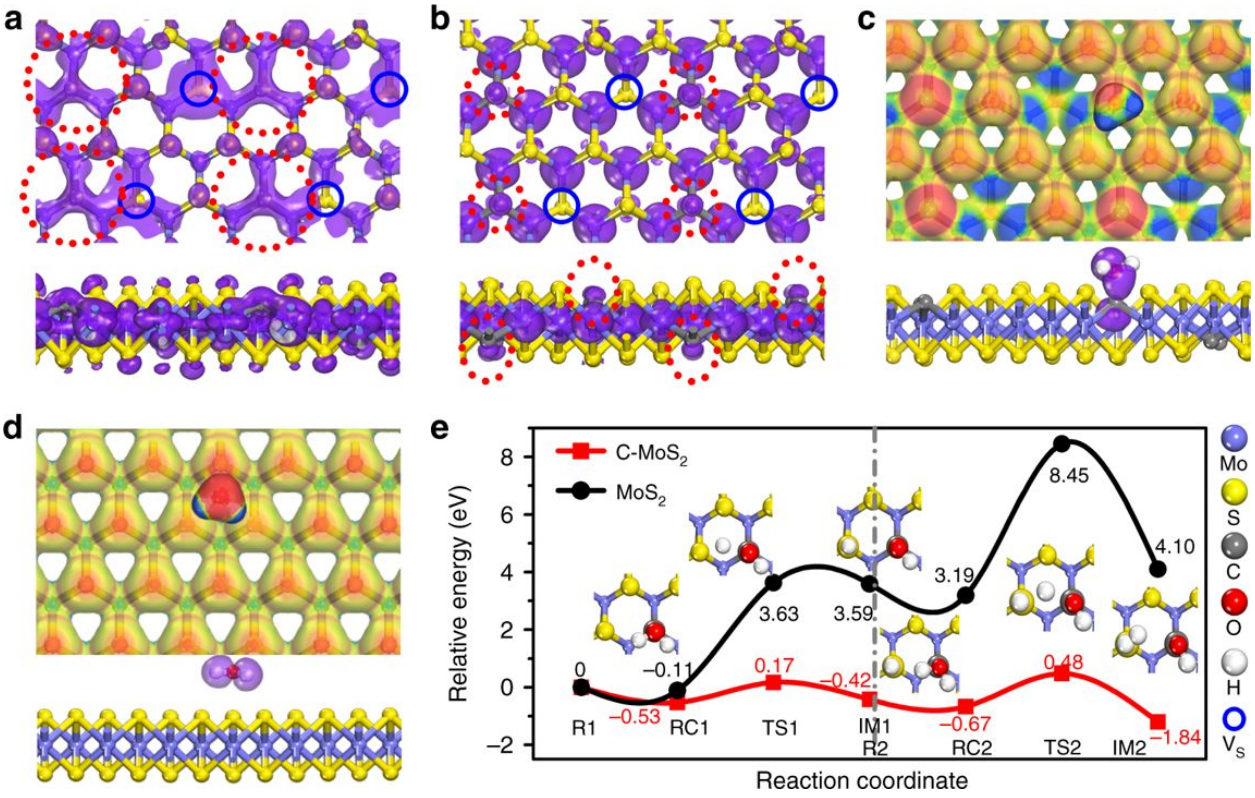

Figure 4. The structural analysis and the reaction pathway of MoS_2 and carbon-doped MoS_2. (a)(b) the top-view and side-view of the sp^2 hybrid orbitals (highlighted by the dashed red circle) of (a) MoS_2 and (b) carbon-doped MoS_2. (c)(d) the top-view and side-view electrostatic potential of adsorbed H_2O on the surface of (c) carbon-doped MoS_2 and (d) MoS_2. (e) the reaction pathway of HER on the surface of MoS_2 and carbon-doped MoS_2. Reprinted from Ref.23, copyright 2019, with permission from Springer.

2.2.2. Constructing a heterogeneous interface

Metal oxides/hydroxides are highly favorable for H_2O dissociation.[98, 99] An effective strategy to promote the kinetics of H_2O dissociation is to integrate them with metal-based HER electrocatalysts. For example, Subbaraman *et al.* deposited nanoscale $Ni(OH)_2$ clusters on the Pt surface, and observed a factor of 8 activity enhancement for HER in alkaline medium, compared to the control sample without metal hydroxides clusters.[24] They attributed the enhancement to the synergistic effect between $Ni(OH)_2$ and Pt, and the proposed schematic is depicted in Figure 5a. The H_2O dissociated on the edges of $Ni(OH)_2$ clusters first, and then the generated H migrated to nearby Pt and recombined with each other to form an H_2 molecule. By introducing Li^+ ions into the compact portion of the double layered hydroxide, the noncovalent interaction (van der Waals interaction) between hydrated cations (AC^+) and adsorbed OH^- leads to the formation of OH_{ad}-$AC^+(H_2O)_x$ complexes, which can induce the destabilization of H-OH bond and further improve the activity (Figure 5c). This is one of the pioneering works in utilizing water dissociation promoters such as $Ni(OH)_2$, to accelerate the kinetics of H_2O dissociation and, thus, enhance the HER activity. Although the authors didn't include theoretical calculation in this work, the proposed mechanism was widely accepted by the scientific community and verified by other groups later.[100-102] This strategy was also extended to other catalytic systems. Niu *et al.* reported a Ni_3N/MoO_2 heterogeneous structure, in which the two materials worked synergistically.[20] DFT calculation revealed that the unoccupied orbital center of MoO_2 is low, which facilitated the H_2O dissociation, while Ni_3N owns a favorable H adsorption activity, with a ΔG_H^* of -0.08 eV. Therefore, MoO_2/NiN_3 heterostructure required only an ultra-small overpotential of 21 mV to achieve a current density of 10 mA cm^{-2}, which is one of the best HER performance. Similar synergistic effect was reported for other systems. Dinh *et al.* also reported a metal/metal oxide heterogeneous

HER electrocatalysts, which showed strong adsorption toward intermediate H and OH^-, respectively, and led to the destabilization of H_2O molecules.[103] The authors tested a series combination of metals and metal oxides and finally identified Ni and CrO_x as the suitable metal and metal oxide. The Ni and CrO_x co-deposited on Cu substrate (denoted as CrO_x/Ni-Cu), which achieved an overpotential of 48 mV at the current density of 10 mA cm^{-2}, one of the best reported HER performances in neutral medium. To verify the destabilization effect induced by the co-existence of Ni and CrO_x, the authors calculated the energy barrier of H_2O dissociation on different surfaces (Cu, Cu-Ni, CrO_x/Cu and CrO_x/Ni-Cu) and found that the energy barrier on CrO_x/Ni-Cu has the smallest value of 0.64 eV.

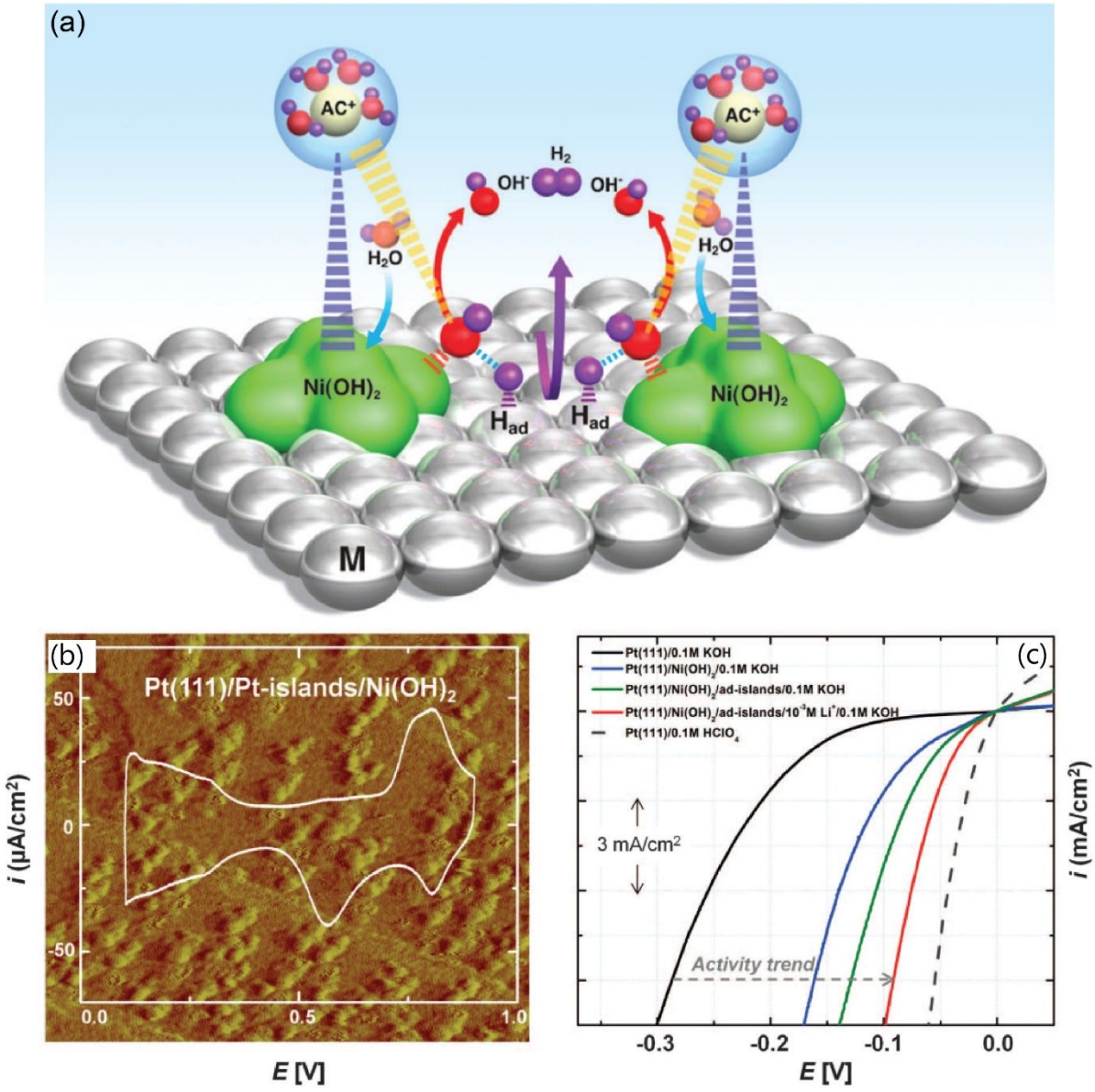

Figure 5. Coupling of $Ni(OH)_2$ with Pt for efficient HER in alkaline medium. (a) the schematic scheme of the working mechanism of $Ni(OH)_2$/Pt heterostructure; (b) the STEM image and cyclic voltammetry (CV) curve of $Ni(OH)_2$/Pt-islands/Pt(111) surface; (c) the HER activity comparison of a series of Pt surfaces modified with different surface structures. Reprinted from Ref.24, copyright 2011, with permission from the American Association for the Advancement of Science.

2.3. Thermodynamic adsorption of OH^-

According to the Brønsted–Evans–Polanyi (BEP) relationship, the energy barrier of a chemical reaction depends on the enthalpy difference between the initial state and the final state.[104-106] When the energy of the final state is lower than that of initial state, the energy barrier is typically lower. This rule also applies to the process of H_2O dissociation. Since the energy barrier of H_2O dissociation relies on the final state energy, it would be affected by the adsorption of intermediate H and OH^-. The thermodynamics of the adsorption of intermediate H on the catalyst surface has been extensively studied and has reached a consensus in the community that an optimal value of ΔG_H^* should be close to 0. Yet, the role of OH^- adsorption has been rarely studied, although it can also significantly affect HER activity. If the adsorption of OH^- on the surface is too strong, while the energy barrier of H_2O dissociation would be lower it could take too much energy to remove the adsorbed OH^- from the surface, which poisons the active sites and slows down the kinetics of HER. On the contrary, if the adsorption is too weak, then the energy barrier of H_2O dissociation would be high and the kinetics of H_2O dissociation would limit HER performance.[25] Therefore, the adsorption of OH^- should also be optimized. Subbaraman *et al.* investigated the HER activity on 3d M(Ni, Co, Fe, and Mn) hydro(oxy)oxide surface and found that it decreases with the strength of M-OH bond (Ni, Co, Fe, and Mn).[84] This relationship is independent of the source of OH^-, no matter whether the OH^- is from the electrolyte or the product of H_2O dissociation. Their work provided a possible strategy to tune the adsorption of OH^- by changing the bond strength of M-OH. The authors also investigated the effect of optimizing the adsorption of OH^- on the surface for hydrogen oxidation reaction (HOR). By introducing more defects on the surface of Ir, the adsorption of OH^- on the surface was facilitated and consequently, the HOR activity was boosted.[85] They also found that PtRu alloy has a higher activity than that of Pt because of the existence of Ru

that facilitates the adsorption of OH^-. The findings on the OH^- adsorption in HOR provide important insights to HER.

2.4. Conductivity

The electrode conductivity of the electrode is determined by three factors, (1) the conductivity of the catalyst, (2) the conductivity of the substrate (or current collector), and (3) the electric contact between the catalyst and substrate. The improvement of any of these three factors could improve the electrode conductivity and, thus, enhance HER activity. A representative example is MoS_2, which has two common phases, semiconducting 2H phase and metallic 1T phase.[26] Lukowski *et al.* reported an exfoliation method to prepare 1T phase MoS_2, which achieved a current density of 10 mA cm^{-2} with an overpotential of 187 mV.[40] This value is much better than that of 2H phase MoS_2 (Figure 6a). The enhanced performance was attributed to the better conductivity of electrocatalyst. Alternatively, if the active catalyst material is less conductive, they are typically deposited on a current collector. There are numerous reports on how to grow catalysts on conducting substrates such as graphene,[107] carbon nanotubes,[108] Ni foam,[109] *etc*. For example, Li *et al.* grew MoS_2 on reduced graphene oxide (RGO) and achieved a small Tafel slope of 41 mV dec^{-1}, which is much smaller than that of MoS_2 nanoparticles without the substrate (Figure 6b).[107] Nevertheless, these three factors are often coupled with each other and it's hard to distinguish the contribution of each factor to the electrode conductivity. For example, the improvement of the conductivity of catalyst or substrate would also reduce the contact resistance between them. Voiry *et al.* studied the effect of contact resistance (R_c) between the substrate and MoS_2 for HER activity.[110] By carefully controlling the treatment of 2H phase MoS_2 with n-butyllithium, 2H phase MoS_2 was converted to 1T phase MoS_2 in different extents and consequently, the R_c was reduced.

As a result, the efficiency of electron injection from the electrode to catalyst was improved. The phase engineered MoS_2 achieved an onset potential of ~ – 0.1 V and a Tafel step of ~50 mV dec^{-1}, comparable to that of 1T phase MoS_2. The authors claimed that the basal plane of 2H MoS_2 with S vacancies is active toward HER, but it is rendered inactive because of the high R_c between the MoS_2 and the substrate. This problem was alleviated by minimizing the R_c. In addition to directly deposit catalyst material onto current collector, avoiding using non-conductive binder such as Nafion, is also important for reducing the R_c between the substrate and the catalyst.[111]

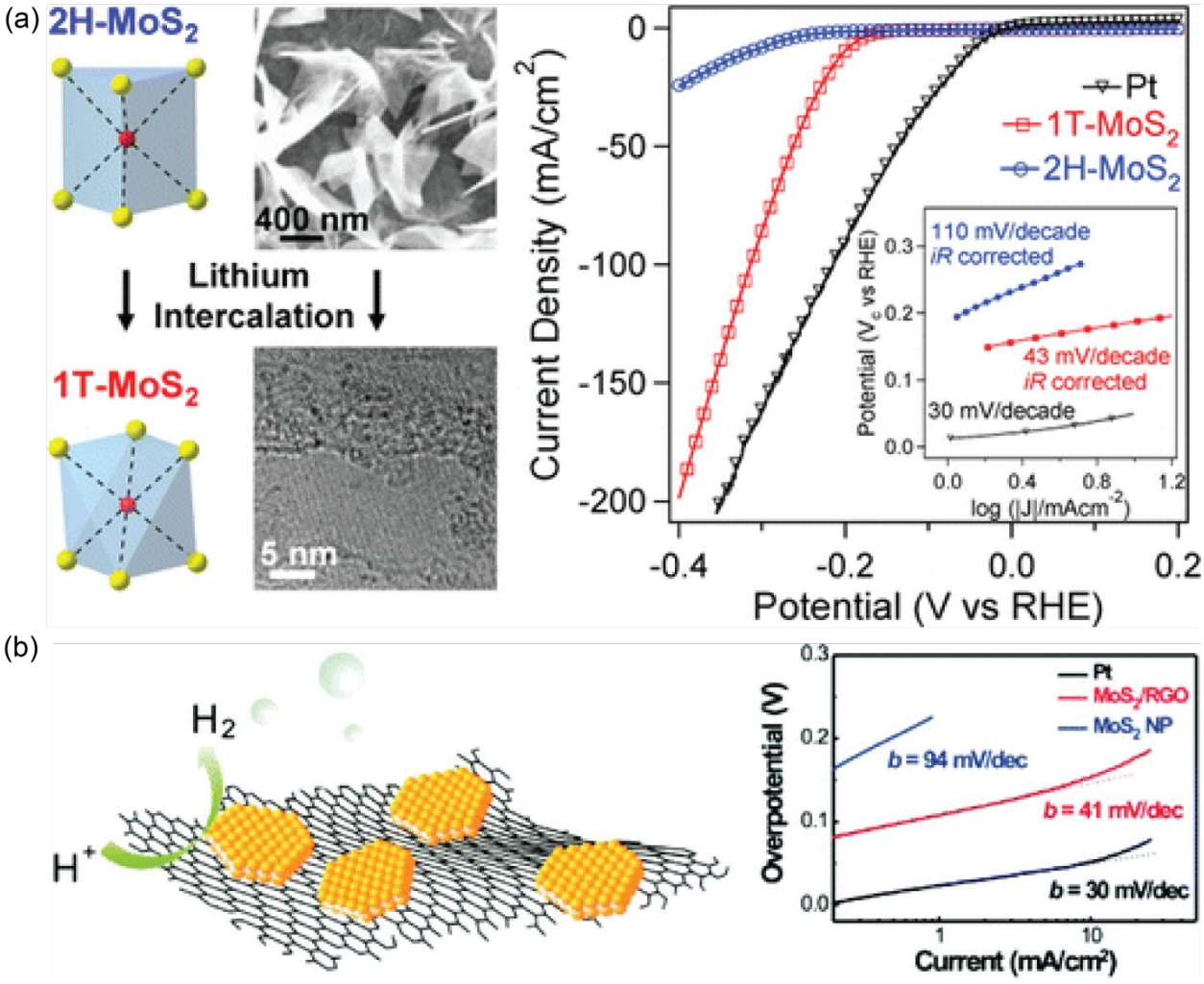

Figure 6. The effect of conductivity on the activity of MoS_2 for HER. (a) phase engineering of MoS_2 from 2H phase to 1T phase to improve its conductivity; (b) coupling MoS_2 with graphene to improve the conductivity of substrate

and electric contact. (a) reprinted from Ref.40, copyright 2013, with permission from American Chemistry Society; (b) reprinted from Ref.107, copyright 2011, with permission from American Chemistry Society

2.5. Charge transfer

Charge transfer between the catalyst surface and electrolyte is another important factor governing the HER activity of electrocatalyst. It can be evaluated by the charge transfer resistance (R_{ct}) extracted from the Nyquist plots by performing electrochemical impedance spectroscopy (EIS).[27] If the Nyquist plot has a semi-circle, the diameter of the circle can be approximated as the R_{ct} value of the system. The larger the diameter, the larger the R_{ct}. R_{ct} is determined by many factors such as the applied potential on the working electrode, the conductivity of catalyst, the contact surface area between catalyst and electrolyte, the conductivity of the electrolyte, *etc*. The improvement of any of these factors would decrease the R_{ct}. For example, the larger the applied potential, the larger the driving force for the transfer of electrons. When the electrode materials have better conductivity, the R_{ct} is also smaller. Increasing the contact surface area between catalyst and electrolyte would also decrease the R_{ct}, because contact resistance is inversely proportional to the surface area of electron transport. Finally, improving the conductivity of the electrolyte, by increasing the concentration of conductive species or using more conductive species in the electrolyte, is also helpful. For example, Patil *et al.* showed that increasing the concentration of KCl electrolyte from 10 mM to 100 mM and final 500 mM, the HER activity of the catalyst increased accordingly.[112]

2.6. Bubble effect

When bubbles generate on the surface of catalysts, they don't detach from the electrode surface immediately. Instead, they attach on the surface of the electrode and grow to a certain size before they leave the surface in the form of bubbles. The covered bubbles will hamper the electron transfer between catalyst and electrolyte, which increases the electric resistance and causes a voltage drop. This effect is called the bubble effect.[64, 113, 114] The bubble effect mainly includes two parts: the surface area reduction by bubble coverage and the formation of a bubble froth layer. Usually, the higher the current density, the higher the bubble coverage on the catalyst surface. Qian *et al.* reported that the ohmic resistance is proportional to the bubble coverage.[115] One of the commonly used approaches to mitigate the bubble effect is to create nanostructures, which make it easier for bubbles to release from the electrode surface. Lu *et al.* synthesized a nanostructured MoS_2 film, which showed a much higher activity toward HER compared to the flat film.[28] The adhesive force measurements found that the adhesive force of bubbles on a nanostructured surface is much smaller than that on the flat surface, as indicated by the smaller bubble size on nanostructured MoS_2 (Figure 7). The second approach to minimize the bubble effect is to make the electrode surface superaerophobic. For example, Hao *et al.* synthesized Cu_3P microsheets and they showed a high activity toward catalyzing HER and OER.[29] The authors measured the contact angle of bubbles on the surface of materials and found that the contact angle on the superaerophobic surface was larger than those of control samples, suggesting that the superaerophobic surface facilitates the detachment of bubbles. However, it is noteworthy that the superaerophobic characteristic also makes it harder for electrolytes to get access to the active sites on the catalyst surface. Therefore, a balance has to be maintained if this strategy is employed.

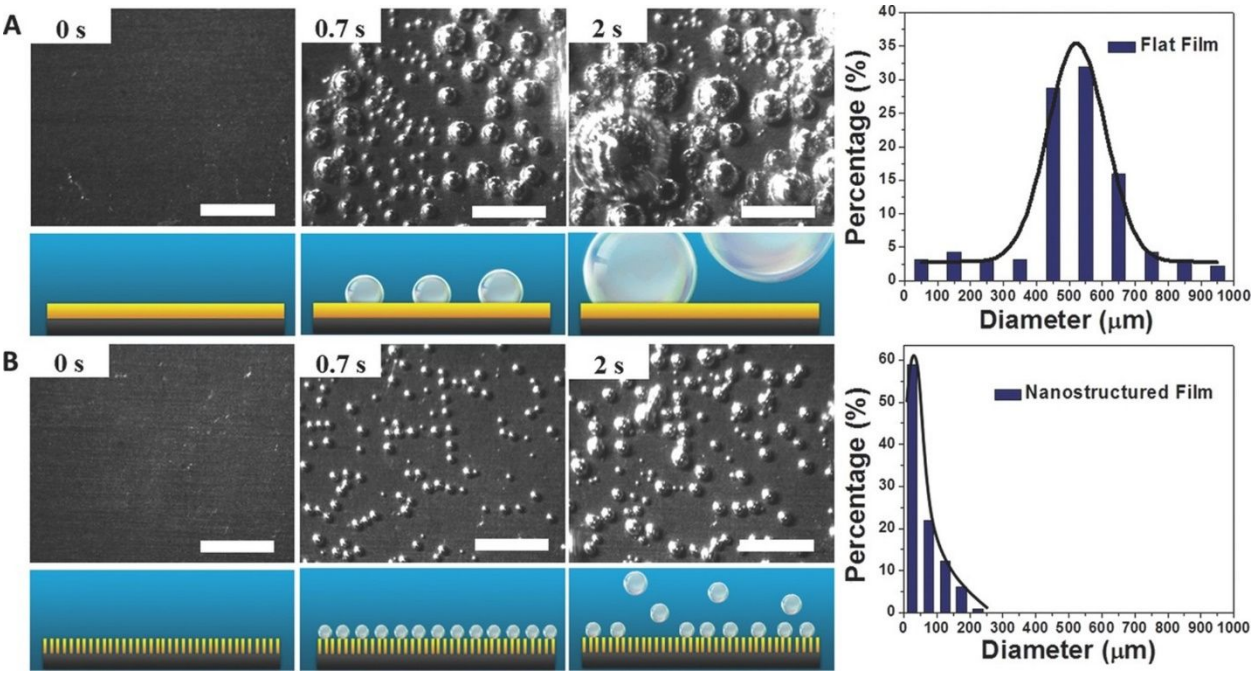

Figure 7. The minimization of the bubble effect by creating nanostructures. Bubbles forming on (A) flat surface and (B) nanostructured surface. Reprinted from Ref.28, copyright 2014, with permission from Wiley-VCH.

2.7. Stability

The stability of electrocatalysts is of great importance for practical application and it has rarely been studied seriously. There are two ways to experimentally characterize the stability of electrocatalysts.[61] The first one is the current-time test. A constant potential is applied and how the current changes with time is recorded. This method is closer to the practical application. The second method is CV cycling, which is also called the accelerated stability test. Using this method, the electrodes are scanned in the HER potential window for a certain number of cycles, and the LSV curves before and after CV cycling are compared with each other. The better overlap of LSV curves before and after CV cycling, the better the stability. It's worth mentioning that both methods are qualitative measurements. Recently, Geiger *et al.* proposed a metric—stability number to

evaluate the stability of electrocatalyst quantitatively.[116] The definition of stability number is the ratio of the amount of evolved gas to the amount of dissolved catalyst. The larger the number, the better the stability. They used this method to study the IrO_2 system for OER and made a quantitative comparison between different samples. However, the application of stability number is limited in certain situations. For example, if the catalyst degradation mechanism is particle aggregation, which doesn't involve particle dissolution, then it's hard to use stability number to evaluate the stability of the catalyst. Theoretically, the stability of electrocatalyst could be simulated by calculating the Pourbaix diagram of the material. In this way, the thermodynamic stable phase under working conditions can be found, but this method cannot take the kinetics of materials evolution into consideration. If the electrocatalyst is transforming from its semi-stable phase to the thermodynamic stable phase under the working conditions and the process is very slow, then the Pourbaix diagram cannot capture this process and will only give the thermodynamic stable phase, which could be misleading. Another way to simulate the stability of the catalyst is to do MD simulation, which however is only able to evaluate the catalyst's stability for a very short-time scale and cannot reflect the activity variation over a long time scale.[117]

There are several mechanisms for the degradation of electrocatalysts, including particle detachment, dissolution, aggregation, and carbon corrosion.[31] One important technique that has been used to probe the degradation mechanism of catalyst is identical location transmission electron microscopy (ILTEM).[118, 119] The same position before and after measurements will be located and compared to reveal the change of catalyst during the tests. For example, Mayrhofe *et al.* found that the absolute number of Pt/C particles decreased a lot after electrochemical tests, while there was only a very small increase of particle size, indicating that a lot of the particles detached from the surface in the electrochemical tests.[118, 119] The dissolution of Pt can also be

observed under ILTEM. Although Pt is very stable, it can still dissolve at pH < 2 and potential beyond 0.85 V vs standard hydrogen electrode (SHE), according to the Pourbaix diagram of Pt (25 ^{o}C).[120] Perez-Alonso *et al.* observed the dissolution of Pt by using ILTEM.[121] They observed that both the number and the size of Pt particles decreased after 3000 degradation cycles between 0.6 V and 1.2 V versus reversible hydrogen electrode (RHE), suggesting the detachment and dissolution of Pt particles. Particle aggregation is another mechanism of catalyst degradation.[30, 122-124] The aggregation of particles is often due to the migration of particles, which can be directly observed under ILTEM. As shown in Figure 8a and b, separate Pt particles aggregate into "string-shape" clusters after electrochemical measurements, indicating the migration caused aggregation of Pt particles. Similar "string-shape", "L-shape" or "T-shape" clusters were observed in other areas under ILTEM. The carbon corrosion is another degradation mechanism.[122, 125, 126] It has been commonly observed in fuel cells since its relatively high operation temperature can speed up the corrosion of carbon support. As a result, the porosity decreases and limits the mass transfer. It is important to point out that multiple degradation processes often occur at the same time during catalytic reactions (Figure 8c and d).

Long-term stability is a very important aspect of any electrocatalysts and extending the lifetime of catalyst is always desired. Some general approaches have demonstrated to be useful in enhancing the long-term stability of HER catalyst. First, the binder-free electrocatalysts are preferred over powdered form catalysts because electrolysis is performed at high currents in practical systems, and powders are more likely to disintegrate from electrode under these conditions. Second, the active phase of HER material should be a thermodynamically stable phase, because the meta-stable phase has the risk of being reduced back to the thermodynamically stable

phase during HER. For example, if Ag_2O is used as HER electrocatalyst, it will be reduced to form metallic Ag during the reaction according to the Pourbaix diagram, and lose its activity.[127] Third, adding a geometric structure could protect relatively unstable components if any. For instance, Hu *et al.* encapsulated few layers of graphene on NiMo nanoparticles and improved its long-term stability in acidic medium. Their data showed that 3–5 graphene layers achieved the best balance between activity and stability.[128] Fourth, using certain pretreatment processes to remove defects, dangling bonds, or surface oxides could also improve catalyst's stability. Ledendecker *et al.* found that by pretreating tungsten carbide (WC) with NaOH to remove native oxide layers, a significant lower dissolution rate was observed under open circuit potential.[129] Nevertheless, it is noteworthy that many defects and surface oxides also exhibit good catalytic activities. Therefore, this strategy is somewhat a trade-off between activity and stability.

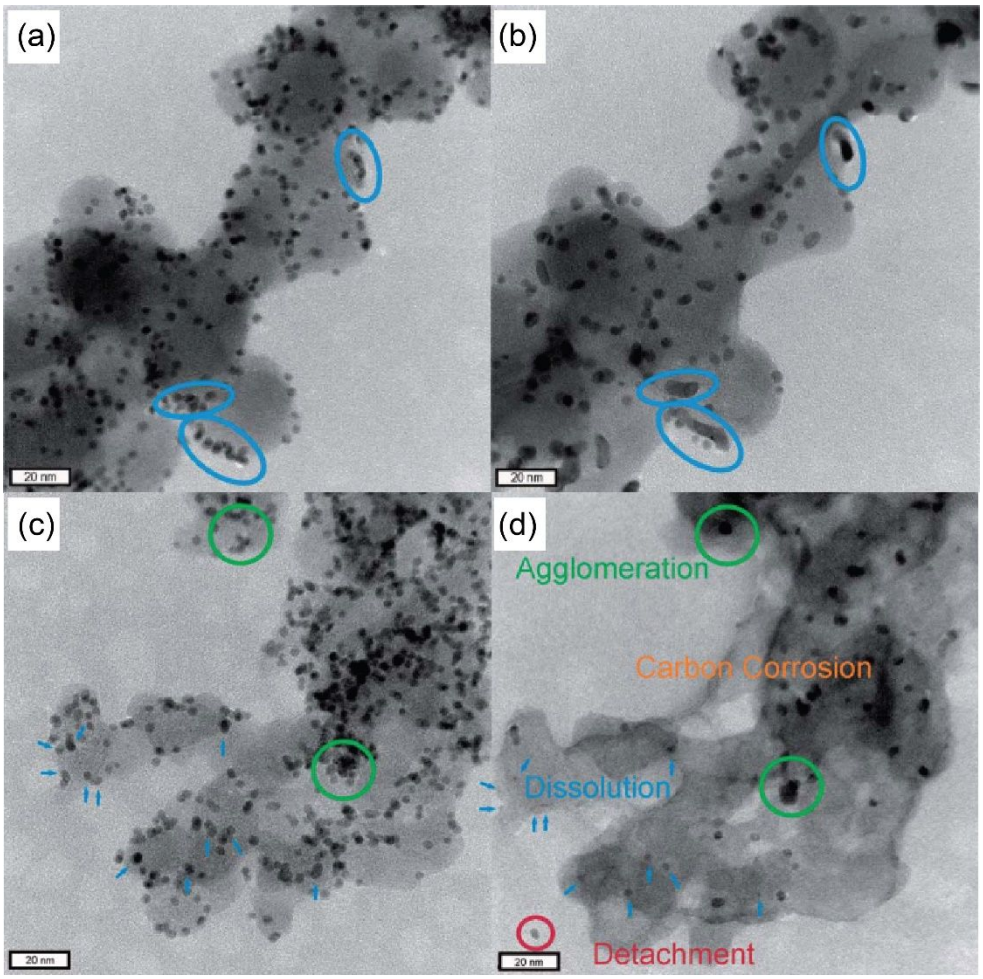

Figure 8. The degradation of catalysts in measurements. (a)(b) the images showing the migration and aggregation of Pt/C (a) before and (b) after 3600 cycles between 0.4 V and 1.4 V vs RHE at a scan rate of 1 V/s in 0.1 M $HClO_4$. (c)(d) the images showing four different degradation mechanisms of Pt/C (d) before and (d) after 3600 cycles between 0.4 V and 1.4 V vs RHE at a scan rate of 1 V/s in 0.1 M $HClO_4$. Reprinted from Ref.31, copyright 2012, with permission from The Royal Society of Chemistry.

3. The power of coupling experiments with DFT for HER

This section discusses the accomplishments made by coupling experiments and DFT in gaining insights into the fundamentals of HER and facilitating the development of new HER electrocatalysts.

3.1. Insights of the fundamentals of HER obtained from DFT

3.1.1. Explanation of experimental phenomena

DFT has been used to explain experimental results, for example, the pH dependence of H binding energy on the surface of Pt. The activity of Pt for catalyzing HER in alkaline medium is two to three orders lower than that in acidic medium.[83] To explain the experimental observation, Cheng *et al.* employed *in situ* DFT calculation by taking the explicit solvent and potential into consideration, and studied the H binding energy dependence over the Pt(100)/H_2O interface.[32] As shown in Figure 9, when pH increases from 0.2 to 12.8 at the potential of +0.3 V vs. RHE, it negatively shifts the potential from 0.29 V to − 0.46 V vs. SHE. As a result, the adsorption of water on the surface was repelled, which in turn increased the adsorption energy of H on the surface of the electrode and consequently decreased the HER activity. This work demonstrated the importance of considering water adsorption or surface hydrophilicity in the design of HER electrocatalyst.

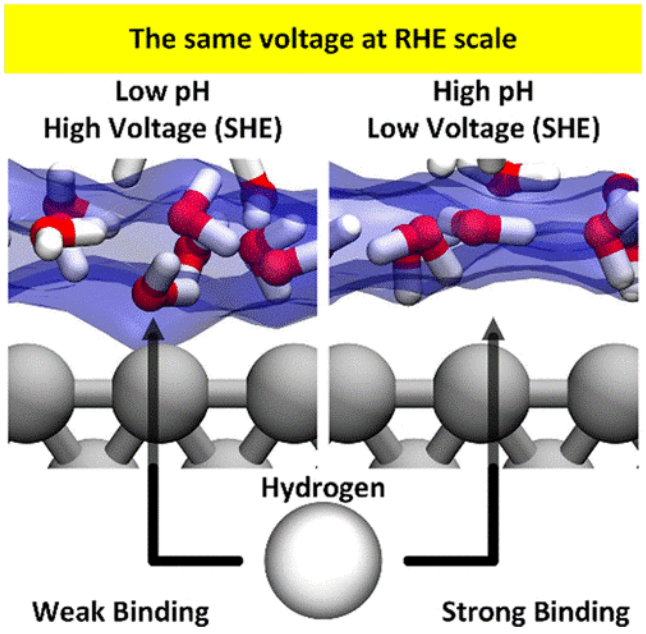

Figure 9. The *in situ* quantum chemistry simulation of the pH dependence of the H binding energy over Pt(100)/H_2O interface. Reprinted from Ref.32, copyright 2018, with permission from the American Chemistry Society.

3.1.2. Prediction of the reaction mechanism of HER

It is noteworthy that the reaction mechanism of HER is expected to be different for different materials. For example, Tang *et al.* studied the mechanism of HER on the basal plane of 1T phase MoS_2 by DFT and the calculated ΔG_H^* indicated that HER probably happened with H coverage between 12.5%~25%.[33] The energy barrier calculation showed that under the H coverage of 25%, the Volmer step is fast with a small energy barrier around 0.16 eV, while Heyrovsky step (with an energy barrier of 0.62 eV) is preferred over Tafel step (with a barrier of 1.07 eV). These values suggested that HER proceeds via the Volmer-Heyrovsky reaction pathway, which is consistent with the measured Tafel slope of 40 mV dec^{-1}. The authors also found that the HER activity of 1T phase MoS_2 would increase when Mo was substituted by some other elements, like Mn, Ni, Fe, *etc*. Huang *et al.* performed the HER mechanistic study on the edge of 2H phase MoS_2.[35] They found that HER took place via the Volmer-Heyrovsky pathway involving an electron-rich molybdenum hydride and a hydronium cation. The estimated energy barrier of 17.9 kcal mol^{-1} is in good agreement with the experimental value of 19.9 kcal mol^{-1} estimated from turnover frequency (TOF). The protonation of the electron-rich Mo hydride is more favorable than the protonation of the hydrogen on sulfur since the electron localized around the Mo-H bond is easier to transfer to form H_2 bond. In the discussion of TMD HER catalysis, S-H has always been considered as an important intermediate. However, the authors found that the S-H bond was not a critical parameter for describing the HER activity since it did not play a direct role in determining the effective energy barrier. On the contrary, the kinetic barriers, instead of equilibrium thermodynamics, are suggested to be the descriptor for evaluating the HER performance, which is

supported by the consistency between the calculated and experimentally determined energy barrier. Huang *et al.* also investigated the reaction mechanism of HER on the basal plane sulfur vacancy site of 2H phase MoS_2 using grand canonical potential kinetics (GCP-K).[34] Both the potential and pH dependence of HER at the sulfur vacancy of the basal plane of 2H phase MoS_2 can be described by using the GCP-K formulation. The authors found that the rate-determining step of HER in both acidic and alkaline medium was the Volmer step, in which the second H was adsorbed from the solution. The GCP-K formulation is able to show that the stretched bond distance changes continuously as a function of the applied potential, which explains the reason of the higher activity in the alkaline medium since the transition state (TS) is closer to the product, leading to a smaller Tafel slope of 60 mV dec^{-1}. Their calculation results also suggested that the second H at the chalcogenide vacant site was the most active one. Based on that, the authors screened the rest of the 2H group VI TMD and found that $MoTe_2$ shows the most promising HER activity.

3.2. Development of new HER electrocatalysts facilitated by DFT

3.2.1. TMD

TMD are a well-studied class of materials for HER due to their low cost and high efficiency.[36, 130] Hinnemann *et al.* found that natural enzymes, hydrogenase enzyme, and nitrogenase enzyme, show high activity toward generating hydrogen. These enzymes have a favorable H adsorption activity compared to Pt, neither too weak nor too strong, with a ΔG_H^* value close to 0 (Figure 10a).[36] They used ΔG_H^* as the descriptor to screen and search for high performance electrocatalysts for HER. The edges of MoS_2 have a ΔG_H^* value close to 0, suggesting its possible high activity toward HER. This hypothesis was confirmed by the experimental results showing that MoS_2 deposited on graphite indeed had a reasonably good HER activity. Their work proved that ΔG_H^* is a good descriptor for searching HER electrocatalysts, and inspired others to

work on MoS_2. Although 2H phase MoS_2 showed a decent activity for catalyzing HER, it is still not comparable to Pt. The reasons include the poor conductivity, low density of active edge sites and low activity of the largely exposed basal planes of 2H phase MoS_2. Therefore, a number of strategies such as improving the conductivity,[40, 131] maximizing the number of active edge sites[36, 42] and activating the inert basal planes of 2H phase MoS_2,[41, 132, 133] have been developed in the past 10 years to improve its HER performance. Among these strategies, here we would like to focus on the strategies of maximizing the number of edge sites and creating amorphous MoS_2.

In order to investigate the active sites of 2H phase MoS_2, Jaramillo *et al.* synthesized MoS_2 nanoplates on Au (111) using a physical vapor deposition method.[42] Figure 10b shows the morphology of synthesized MoS_2 under a scanning tunneling microscope (STM). They found that the HER activity of MoS_2 is not proportional to the area of MoS_2 nanoplate. Instead, it is proportional to the edge length of MoS_2 (Figure 10c and d), which suggests that the edges of 2H phase MoS_2 are the active sites for HER. This pioneering work motivated a lot of follow up studies to engineer the structure of MoS_2, aiming to maximize the number of edge sites. For example, Kong *et al.* grew vertically aligned MoS_2 thin film on a substrate and exposed the maximum amounts of edge sites.[56] Kibsgaard *et al.* reported a highly-ordered double-gyroid MoS_2 structure with edge sites preferentially exposed, which showed high activity toward HER.[57] Another approach to enhance the activity of MoS_2 is to synthesize amorphous structure.[134] Defects are created in the structure when the long-range ordering in amorphous MoS_2 is destroyed. Defect sites usually show good HER activity. For example, Vrubel *et al.* synthesized amorphous MoS_{2+x} by electrodeposition. The amorphous MoS_{2+x} achieved a current density of 20 mA cm^{-2} at a small overpotential of 170 mV.[135] The undercoordinated S in amorphous MoS_{2+x} are similar to the edge sites in crystalline 2H phase MoS_2 and are the possible active sites for catalyzing HER.[136]

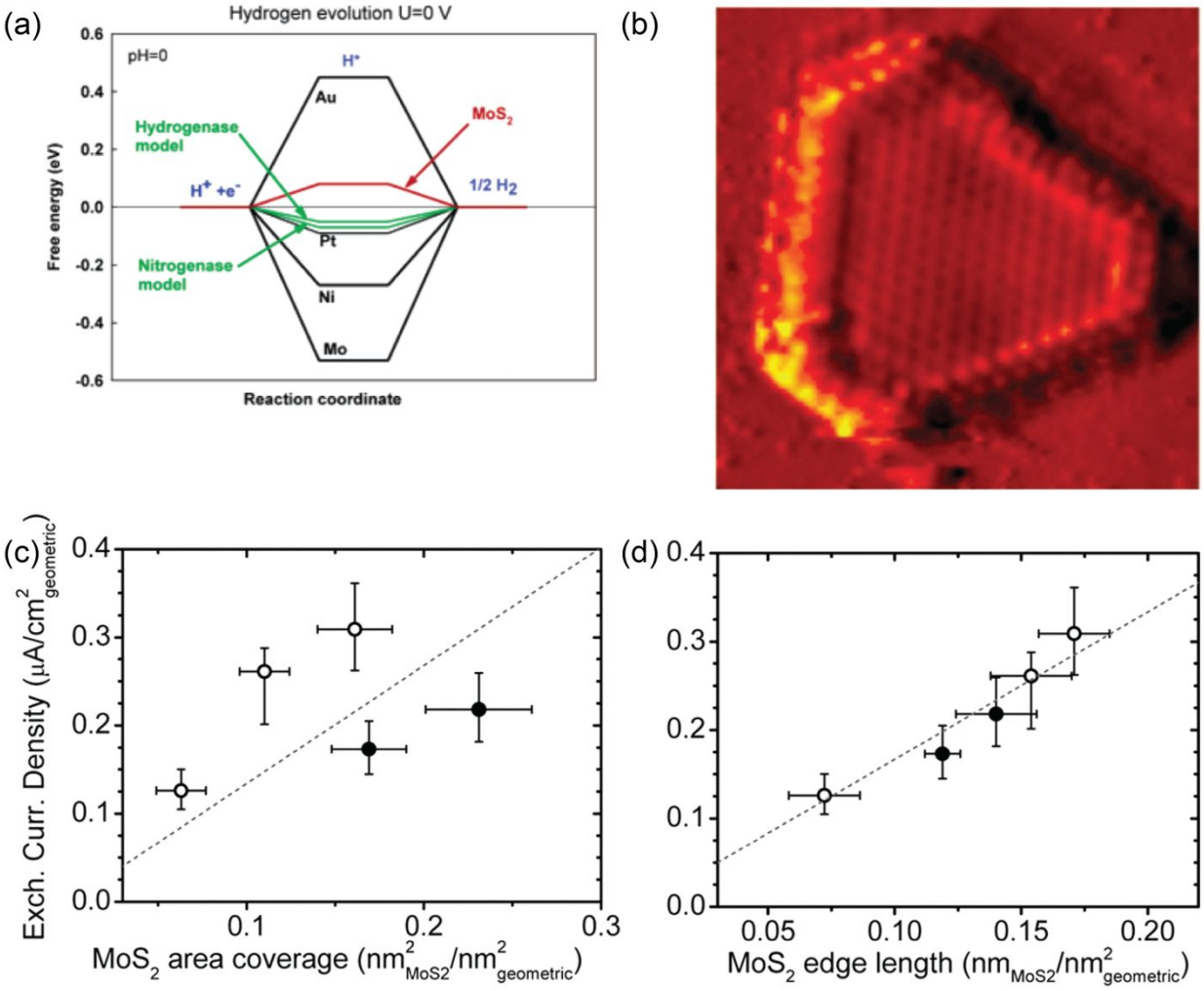

Figure 10. MoS_2 as electrocatalyst for HER. (a) the ΔG_H^* of Au, Pt, Ni, Mo, hydrogenase, nitrogenase models and MoS_2; (b) the morphology of physical vapor deposited MoS_2 under STM; (c)(d) the activity correlation of MoS_2 with (c) area coverage and (d) edge length. (a) reprinted from Ref.36, copyright 2005, with permission from the American Chemistry Society. (b)(c)(d) reprinted from Ref.42, copyright 2007, with permission from the American Association for the Advancement of Science.

3.2.2. Carbon-based materials

Carbon-based materials are attractive HER catalysts due to their low cost and high abundance.[137] Besides, compared to the metal-based catalysts, they have better corrosion and oxidation resistivity, which is significant for practical applications. However, pristine carbon-

based materials are known to be inert for HER. Doping engineering methods have been reported to activate the catalytic activities of carbons under the guidance of DFT. DFT calculations revealed that by co-doping graphene with N and P atoms, the ΔG_H^* can be switched from a positive value to close to 0.[137] Zheng *et al.* synthesized and reported the HER performance of N and P co-doped graphene (N,P-G). Obvious performance enhancement was observed for the N,P-G compared to the undoped graphene sample. Since then, a number of follow-up works of using doped carbon materials as HER electrocatalysts have been reported.[37, 138-140] For example, Zheng *et al.* also coupled graphitic-carbon nitride (g-C_3N_4) with nitrogen-doped graphene (NG).[37] g-C_3N_4 has favorable H adsorption active sites, while the presence of NG facilitates charge transfer. The hybrid material achieved a current density of 10 mA cm^{-2} at an overpotential of ~ 240 mV and a Tafel slope of 51.5 mV dec^{-1}. These were the best values reported for carbon-based HER electrocatalysts back to then. Jiao *et al*. systematically investigated the role of different doping on the HER activity of carbon-based materials via a combination of DFT calculation, spectroscopic characterization, and electrochemical measurements.[140] The authors fitted the highest peak position (E_p) of DOS of the doped carbons with respect to ΔG_H^* and found that for a graphene surface, the higher the E_p, the stronger H adsorbs on the surface. The interaction of H with the surface of graphene splits the hybridized energy states into two parts: the antibonding states, which usually cross the Fermi level, and the bonding states, which usually are below the Fermi level. The bonding strength of H on the surface is usually determined by the filling of the antibonding states. A higher energy of E_p means that the highest peak position is closer to the Fermi level, which moves up the antibonding states with a lower occupancy, stabilizing the bonding of H. Since the adsorption of H on the graphene surface is usually weak, the stronger bonding of H on the surface shifts ΔG_H^* closer to 0, corresponding to a higher activity. The ΔG_H^* of different dual heteroatom doped graphene were

well correlated with the experimental results, showing an activity order of N,S-G > N,P-G > N-G > N,B-G. Their work demonstrated that the activity of carbon-based materials can be boosted by tuning the electronic structure via rational heteroatom doping.

3.2.3. Single-atom catalysts

The concept of single-atom catalysts (SACs) is proposed because of the desire to achieve 100% utilization of metal atoms and reduce the cost of catalysts. Qiao *et al.* demonstrated the first synthesis of single-atom Pt anchored FeO_x, denoted as Pt_1/FeO_x SAC, which showed a high activity for oxidizing CO.[38] DFT calculations found that the charge transfer between Pt and FeO_x made the Pt highly positive and gave it more vacant d orbitals, which stabilized the anchoring of Pt on FeO_x and decreased the activation energy barrier for CO oxidation. SACs have been used for other catalytic reactions, like HER,[25, 141-143] ORR,[144-146] *etc*. Cheng *et al.* utilized the atomic layer deposition (ALD) method and successfully dispersed single platinum atoms and clusters onto the N doped graphene nanosheets (NGNs).[141] Single Pt anchored NGNs showed much higher activity and stability for HER compared to the commercial Pt/C catalyst. DFT calculations indicated that the charge transfer induced partially unoccupied 5d orbitals of Pt is the reason for the extraordinary performance. Deng *et al.* reported a single Pt atom doped MoS_2, denoted as Pt/MoS_2.[142] DFT calculations revealed that the single atomic Pt doping can facilitate the adsorption of H on in-plane S sites neighboring to Pt sites. The authors also computed a series of different metal-doped MoS_2 systems and plotted a volcano based on their ΔG_H^* values, which was consistent with their experimental results on HER activity. Jiang *et al.* synthesized a nanoporous cobalt selenide with Co vacancies (denoted as np-$Co_{0.85}Se$), which helped anchor the single Pt in $Co_{0.85}Se$ (denoted as Pt/np-$Co_{0.85}Se$) (Figure 11).[143] Pt/np-$Co_{0.85}Se$ showed a high HER activity in neutral

medium. The operando XAS revealed a peak corresponding to the Co-OH bond forming under the working environment, suggesting the single Pt doping can activate the nearby Co for H_2O dissociation. DFT calculation revealed that the Pt/np-$Co_{0.85}Se$ has a smaller H_2O dissociation energy barrier of 0.491 eV, compared to np-$Co_{0.85}Se$ (0.881 eV). Additionally, Pt/np-$Co_{0.85}Se$ has more favorable H adsorption sites than that of $Co_{0.85}Se$. The improved H adsorption and H_2O dissociation together lead to a high HER activity.

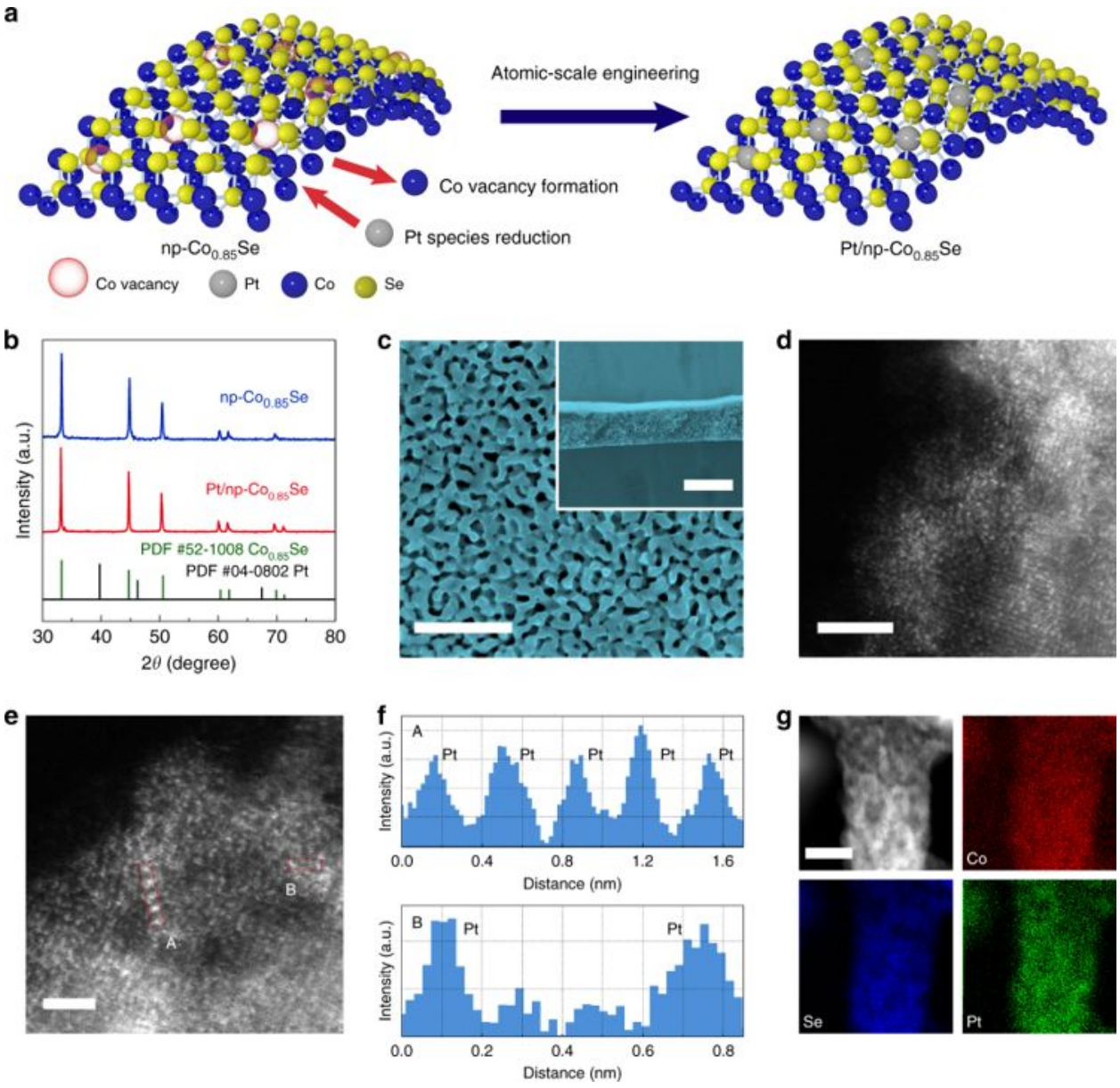

Figure 11. The synthesis and characterization of Pt/np-$Co_{0.85}Se$. (a) Schematic scheme of the synthesis procedures; (b) X-ray diffraction (XRD) of synthesized np-$Co_{0.85}Se$ and Pt/np-$Co_{0.85}Se$; (c) scanning electron microscope (SEM) of Pt/np-$Co_{0.85}Se$ and the inset shows the cross-section of Pt/np-$Co_{0.85}Se$; (d)(e) HAADF-STEM images of Pt/np-$Co_{0.85}Se$ under different resolutions; (f) the line-scanning intensity profile obtained from the area highlighted by the red box in Figure (e); (g) the scanning transmission electron microscopy-energy dispersive X-ray (STEM-EDX) mapping of Pt/np-$Co_{0.85}Se$. Scale bar: c 500 nm, inset: 20 μm. d 2 nm. e 1 nm. g 10 nm. Reprinted from Ref.143, copyright 2019, with permission from Springer.

3.2.4. MXene

MXene were first discovered by Naguib *et al.* and they got the name of MXene because of its "graphene" like property.[147] MXene is usually synthesized by exfoliating MAX with HF followed by sonication, among which M are early transition metals, A are mostly group 13 or 14 elements (Al or Ga), and X are usually carbon or nitrogen. The first example of using MXene as HER electrocatalyst was reported by Seh *et al.*.[39] DFT calculation predicted that Mo_2CT_x is a promising HER electrocatalyst. First, the H adsorption energy of Mo_2CT_x is in a position closer to the top of the "Volcano plot". Second, the basal plane of two dimensional Mo_2CT_x was active for H adsorption, which is different from MoS_2 whose edges are the active sites. Therefore, Mo_2CT_x has more active sites per unit area compared to that of MoS_2. Two-dimensional MXene have been used as electrocatalysts for different reactions, including HER, OER, ORR, *etc*.[44, 148, 149] Gao *et al.* employed DFT calculation to study a series of two-dimensional MXene materials, and found that MXene such as Ti_2C, V_2C, and Ti_3C_2, are all conductive under standard conditions, which allows efficient charge transfer during HER.[44] Besides, the surface Pourbaix diagram indicated that MXene are typically terminated by oxygen or hydroxyl groups, which have a favorable ΔG_H^* close to 0. Their computational work inspired numerous experimental works on developing MXene for

HER electrocatalysts.[150, 151] For example, Kuznetsov *et al.* synthesized a single Co doped 2D Mo_2C structure (denoted as Mo_2CT_x:Co) that showed an excellent HER activity. EXAFS studies revealed that Co occupy the Mo sites and activate the terminated oxygen ions for H adsorption.[150] Zhang *et al.* synthesized $Mo_2TiC_2T_x$ with abundant exposed basal planes and Mo vacancies.[151] Mo vacancies help immobilize Pt atoms, and the single Pt doped $Mo_2TiC_2T_x$ (denoted as $Mo_2TiC_2T_x$–Pt_{SA}) showed an impressive high mass activity, which is about 40 times higher than that of commercial Pt/C catalyst. The DFT calculation unveiled that the favorable H adsorption activity on $Mo_2TiC_2T_x$–Pt_{SA} is the origin of its high HER activity.

MXene surface has various possible terminations and, therefore, their properties are highly tunable.[152-155] For example, Handoko *et al.* combined both experimental and theoretical approaches to investigate the effect of 5 different basal plane functionalization (T_x) on the HER activity.[152] They found that the higher fluorine coverage on the basal plane, the lower the HER activity. Their results indicated that the oxygen terminations of MXene are catalytically active toward HER, which is different from the case of 2H phase TMD such as MoS_2, in which only the edge sites are active. The effect of transition metal modifications on the activity of M_2XO_2 was also studied by first principles screening.[153] Li *et al.* found that although the majority of pristine MXene showed a weak HER activity, transition metal surface modification can greatly enhance their HER activity. The presence of transition metal not only optimizes ΔG_H^* but also reduces the H_2 production activation barrier. A HER reaction mechanism switch from Volmer–Heyrovsky pathway to Volmer–Tafel pathway was observed after MXene were modified with TM adatoms. A table (table 1) summarizing the state-of-the-art HER electrocatalysts is listed below.

Table 1. HER performance of representative state-of-the-art HER electrocatalysts.

Category	Catalyst	Electrolyte	η (mV)@10 mA cm^{-2}	Tafel slope (mV dec^{-1})
TMO	C-$Ni_{1-x}O$[60]	1.0 M KOH	27	36
	NiO/Ni-CNT[156]	1.0 M KOH	~90	~75
	NiO NRs-m-Ov[157]	1.0 M KOH	110	100
	Ni/NiO-250[158]	1.0 M KOH	145	43
	Ni, Zn dual doped CoO[159]	1.0 M KOH	53	47
	Ni/NiO@C-2[101]	1.0 M KOH	64	55
	NiO_x@BCNTs[160]	1.0 M KOH	79	119
TMS	N doped Ni_3S_2[69]	1.0 M KOH	155	113
	Ni_3S_2/NF[161]	1.0 M KOH	223	N/A
	Ni_3S_2[162]	1.0 M KOH	335	97
	$NiCo_2S_4$/NF[163]	1.0 M KOH	210	58.9
	Ni_3S_2 NW[164]	1.0 M KOH	199	106.1
	N-NiS/MoS_2[165]	1.0 M KOH	71	79
	MoNiS@NiS/CC[166]	0.5 M H_2SO_4	33	80
	A-RuS_2[167]	0.5 M H_2SO_4	141	65.6
TMD	porous MoS_2 film[57]	0.5 M H_2SO_4	150	50
	single-layer MoS_2[168]	0.5 M H_2SO_4	185	45
	SE-MoS_2 film[169]	0.5 M H_2SO_4	104	59
	monolayer MoS_2[170]	0.5 M H_2SO_4	226	98
	MoS_2@C[171]	0.5 M H_2SO_4	136	78
	porous 1T MoS_2 NSs[172]	0.5 M H_2SO_4	153	43
	P-MoS_2 NSs[173]	0.5 M H_2SO_4	43	34
	Ni-Co/1T-MoS_2[174]	0.5 M H_2SO_4	70	38
	1T $MoSe_2$[175]	0.5 M H_2SO_4	152	52
	$MoSe_2$/SMCNT[176]	0.5 M H_2SO_4	100	63
	B-$MoSe_2$ NSs[177]	0.5 M H_2SO_4	84	39
	MoSSe nanodots[178]	0.5 M H_2SO_4	140	80
	1T WS_2 NSs[179]	0.5 M H_2SO_4	142	70

	Co-$WS_2/W_{18}O_{49}$[180]	0.5 M H_2SO_4	210	49
	FeS_2-RGO film[181]	0.5 M H_2SO_4	139	66
	OGNs@MoS_2[182]	0.5 M H_2SO_4	118	73
	MoS_2/Ni_3S_2[183]	0.5 M H_2SO_4	98	61
	Ni–Mo–S[184]	0.5 M H_2SO_4	200	85
	$(Fe_xNi_{1-x})_9S_8$[185]	0.5 M H_2SO_4	138	82
	$FePSe_3$/NC[186]	0.5 M H_2SO_4	70	53
Carbon-based materials	N,S-doped graphene[187]	0.5 M H_2SO_4	280	80.5
	EDA-CNTs[188]	0.5 M H_2SO_4	150	116
	N,P-doped graphene[137]	0.5 M H_2SO_4	420	91
	N,P-doped graphene[137]	1.0 M KOH	480	145
	N,S-doped CNT[189]	1.0 M KOH	450	133
	N,P-doped C NWs[190]	0.5 M H_2SO_4	163	89
	3D graphene NWs[59]	0.5 M H_2SO_4	107	64
	g-C_3N_4/graphene[191]	0.5 M H_2SO_4	207	54
	C_3N_4@NG[37]	0.5 M H_2SO_4	240	51.5
SACs	Pt–MoS_2[142]	0.1 M H_2SO_4	~150	96
	400-SWMT/Pt[192]	0.5 M H_2SO_4	27	38
	PtSA-NT-NF[193]	1.0 M PBS	24	30
	Pt SAs/DG[194]	0.5 M H_2SO_4	23	25
	$Mo_2TiC_2T_x$-Pt_{SA}[151]	0.5 M H_2SO_4	30	30
	Pt@PCM[195]	0.5 M H_2SO_4	105	65.3
	Pt@PCM[195]	1.0 M KOH	139	73.6
	Pt_1–MoO_{3-x}[196]	0.5 M H_2SO_4	23.3	28.8
	Pt SASs/AG[197]	0.5 M H_2SO_4	12	29.33
	SANi-PtNWs[198]	1.0 M KOH	70	60.3
	Pt/np-$Co_{0.85}Se$[143]	1.0 M PBS	55	35
	Pd–MoS_2[199]	0.5 M H_2SO_4	78	62
	Pd/Cu–Pt NRs[200]	0.5 M H_2SO_4	22.8	25
	Ru SAs@PN[201]	0.5 M H_2SO_4	24	38
	Ru@Co SAs/N–C[202]	1.0 M KOH	7	30

	Pt–Ru dimer[203]	0.5 M H_2SO_4	~20	28.9
	Fe/GD[204]	0.5 M H_2SO_4	66	37.8
	Ni/GD[204]	0.5 M H_2SO_4	88	45.8
	A–Ni–C[205]	0.5 M H_2SO_4	34	41
	Co–NG[206]	0.5 M H_2SO_4	147	82
	Co1/PCN[207]	1.0 M KOH	138	52
	Co SAs/PTF-600[208]	0.5 M H_2SO_4	94	50
	$Mo_1N_1C_2$[209]	0.5 M H_2SO_4	154	86
	$W_1N_1C_3$[210]	0.5 M H_2SO_4	105	58
MXene	Mo_2CT_x[152]	0.5 M H_2SO_4	189	75
	F-terminated Ti_2CT_x[211]	0.5 M H_2SO_4	170	100
	O-terminated Ti_2CT_x[212]	0.5 M H_2SO_4	190	60.7
	N-Ti_2CT_x[213]	0.5 M H_2SO_4	215	67
	$Ti_3C_2T_x$ nanofibers[214]	0.5 M H_2SO_4	169	97
	$Ni_{0.9}Co_{0.1}$@Nb-$Ti_3C_2T_x$[215]	1.0 M KOH	43.4	116
	Pt/$Ti_3C_2T_x$-550[216]	0.1 M $HClO_4$	32.7	32.3
	TBA-$Ti_3C_2T_x$-Pt-20[217]	0.5 M H_2SO_4	70	65
	Co-MoS_2@Mo_2CT_x[218]	1.0 M KOH	112	82
	MoS_2⊥Ti_3C_2[219]	0.5 M H_2SO_4	110	~40
	$Ni_{0.9}Fe_{0.1}PS_3$@ $Ti_3C_2T_x$[220]	1.0 M KOH	196	114
	MoS_2/Ti_3C_2-MXene@C[221]	0.5 M H_2SO_4	135	45
	$Mo_2TiC_2T_x$-Pt_{SA}[151]	0.5 M H_2SO_4	30	30
	CoP@3D Ti_3C_2T[222]	1.0 M KOH	168	58

4. The limitations and progress of coupling experiments with DFT

Although significant research accomplishments have achieved, there are still challenges in coupling experiments with DFT. In this section, we will discuss the limitations and technical issues and review the progress made in the past few years.

4.1. Experimental measurements

The measured "activity" of HER electrocatalyst could vary a lot depending on the experimental measurement conditions. Using a standardized measurement practice would be therefore critical for evaluating the catalyst's activity and making a fair comparison between the experimental and simulated results. For example, the overpotential required to achieve a geometry current density of 10 mA cm^{-2} (η_{10}) has often been used to compare the activity between different catalysts. η_{10} can be extracted from linear scan voltammetry (LSV). However, the current obtained from LSV includes two parts, faradic current and capacitive current. As shown in the following equation, capacitive current increases with scan rate:

$$I = I_{faradic} + I_{capacitive} = I_{faradic} + \frac{dQ}{dt} = I_{faradic} + \frac{dQdV}{dV\,dt} = I_{faradic} + C \times (scan\ rate) \quad (9)$$

The change of $I_{faradic}$ with scan rate is small compared to that of $I_{capacitive}$ and, therefore, $I_{faradic}$ should be treated as a constant. Although the real system is better to be treated as a constant phase element (CPE) instead of a capacitance,[223] the above equation can still qualitatively explain why current increases with scan rates. In order to minimize the effect of scan rate and obtain the real faradic current, it is recommended to measure the steady-state current with a dwell time of at least 5 minutes under different potentials.[61]

Determination and comparison of intrinsic activity between different HER electrocatalysts are imperative, however, they have rarely been reported in the literature. There are two ways to evaluate the intrinsic activity of electrocatalysts. First, instead of normalizing the current density (j) to the geometry surface area, j can be normalized to the mass of active catalysts or the electrochemical surface area (ECSA). These normalized current densities are called mass activity and specific activity, respectively (Figure 12a).[45] Depending on the structural features and mass loading of the catalyst, different metrics should be used to get a fair and accurate comparison. Among these methods, the value of the specific activity is determined by the ECSA, which is proportional to the total number of available active sites, which is a fair and accurate way to compare the intrinsic activity between different catalysts. The second way is to compare the catalyst's TOF, which is defined by the number of the desired product (in the case of HER, it is H_2 molecule) catalyzed per active site per unit of time.[61] The key of calculating the specific activity and TOF is how to get a precise value of ECSA. There are different methods to measure ECSA such as the non-faradaic double layer capacitance (C_{DL}) method, Brunauer-Emmett-Teller (BET) method, surface redox reactions method, *etc*.[45] Among them, C_{DL} method is currently the most widely used for measuring ECSA. The main uncertainty of using C_{DL} method stems from the uncertainty in determining specific capacitance (C_{spec}), a quantity which varies from one material to another. Even for the same material, different growth methods can sometimes lead to different C_{spec} values. For example, the C_{spec} of (100)-oriented $La_{0.6}Sr_{0.4}MnO_3$ thin-film was measured to be 77 $\mu F\ cm^{-2}$,[224] which is higher than 40 $\mu F\ cm^{-2}$,[225] a widely accepted value for metal oxides in literature. Another uncertainty in the determination of C_{spec} is the possible current contributions from other side reactions (even in the non-faradaic reaction potential window) such as adsorption/desorption of H, intercalation, corrosion, *etc*.[226] These side reactions may lead to

overestimation of the double layer capacitive current. In addition, the electrical conductivity of the material can also affect the accuracy of the C_{DL} method.[227] As shown in Figure 12b, the ECSAs of 16 metal oxides measured by the C_{DL} method are displayed and compared to the values obtained from BET measurement, a method based on physical adsorption of gas molecule on a solid surface. The results showed that the ECSAs of metal oxides with a high electrical conductivity, like IrO_2, RuO_2, $LaNiO_3$ and $LaCoO_3$, are pretty close to the values obtained from BET method, while the ECSAs of those with poor electrical conductivity deviate significantly from the BET determined values. Therefore, it is important to know that C_{DL} method is not perfect and should be used cautiously to measure the ECSA of electrocatalysts.

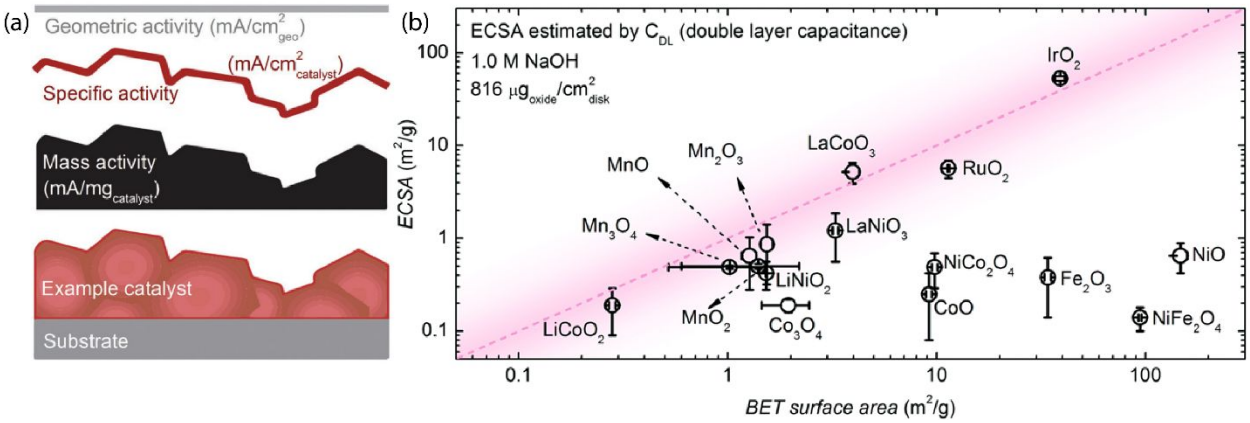

Figure 12. A model of ECSA and different methods to calculate the ECSA. (a) schematic picture showing the difference between geometry activity, specific activity, and mass activity. (b) The comparison between the C_{DL}-estimated ECSAs of 16 metal oxide powders (assuming a specific capacitance of 40 $uF\ cm_{oxide}^{-2}$) and the surface areas measured by the Brunauer–Emmett–Teller (BET) method. Reprinted from Ref.45, copyright 2019, with permission from the American Chemistry Society.

4.2. Characterization

Accurate structural information is the key to build accurate and reliable DFT models. Yet, most of the time catalysts are characterized in an environment that is different from the conditions in the catalytic reaction. As a result, inaccurate information could be obtained. To solve this problem, *operando* characterization techniques that can collect structural and activity/selection information during catalysis simultaneously, have been developed.[228, 229] They are powerful in determining the real active sites and correlating structure properties with catalytic activity. For example, Hu *et al.* observed that the catalytic activity of 2D nanosheets of a Ni-S coordination polymer was getting better during CV cycling (Figure 13).[230] The *in situ* XAS studies unveiled that the increased activity is because of the transformation of the Ni-S coordination polymer into an ultrathin Ni nanosheets with a trace amount of S adsorbing on the surface. Kornienko *et al.* used operando XANES and Raman to monitor the change of CoS_x during the HER process.[231] They found that CoS_x catalyst was converted to CoS_2-like structure under cathodic potential. The high activity of CoS_x was believed to originate from the exposed S sites around those Co ions, which might establish different binding strength compared to the sites in bulk CoS_x. Cao *et al.* used operando XAS to investigate the evolution of a single cobalt doped catalyst and confirmed the formation of a high-valence HO—Co1—N2 moiety due to the interaction between Co-N4 structure and hydroxide.[207] This HO—Co1—N2 structure could further interact with H_2O molecules and serve as H_2O dissociation active sites. The use of XAS helped identify the intrinsic active sites of this single cobalt doped catalyst. Casalongue *et al.* combined *in situ* ambient pressure X-ray photoelectron spectroscopy (APXPS) with DFT calculation and successfully determined the HER active sites of MoS_3.[232] MoS_3 was gradually reduced to MoS_2 during the HER process, accompanied with an activity enhancement, indicating that MoS_2 was the active phase for HER. Deng *et al.* reported the operando Raman spectroscopy on amorphous MoS_x.[46] Under cathodic

potential, a peak at 2530 cm^{-1} corresponding to the S-H stretching vibration mode was observed in operando Raman spectroscopy (Figure 14). In addition, the absence of Mo-H stretching mode excluded the possibility of Mo serving as the active sites for HER. Another interesting phenomenon observed under operando Raman spectroscopy was that Raman signal of S-H stretching vibration mode appeared as early as +0.18 V vs RHE, which indicated the Volmer step (proton discharge step) happened prior to the standard potential of H_2 evolution (0 V vs RHE), but the adsorbed H didn't desorb from the surface in the form of H_2 until -0.15 V vs RHE. It indicated that the H desorption step is the RDS, which is consistent with the experimentally measured Tafel slope of 40 mV dec^{-1}. DFT calculation further showed that only non-apical S sites in the MoS_x structure were active for HER. Another technique that has been used to probe the catalytic active sites is direct instrumental identification. For example, Jonas *et al.* employed an electrochemical scanning tunneling microscope (EC-STM) to study the HER on Pd islands covered Au (111) surface.[233] They observed the largest tunneling current on the boundary of Au and Pd, the smallest current on Au and intermediate current on the Pd surface. This is in good agreement with the fact that HER activity is higher on the Pd islands deposited Au (111) surface compared to pure Au (111) surface and many layer Pd deposited Au (111) surface.

To summarize, these operando techniques, including XAS (XANES and EXAFS), XPS and Raman (or IR), are extremely useful in the determination of active sites and catalytic mechanism. Operando XANES is able to determine the oxidation states of the catalyst.[207] EXAFS analysis with the proper fitting is able to investigate the coordination environment of the active sites in the material, including the coordination number and coordinating species. The challenge is to distinguish the signal from the bulk and surface of the catalyst. Operando APXPS is complementary to the XAS techniques since it extracts only the chemical information on the

surface.[232] Finally, if the catalyst contains X-H bonds, then operando Raman (or IR) spectroscopy would be highly favorable because of its high sensitivity to the vibrational mode of X-H bond.[46]

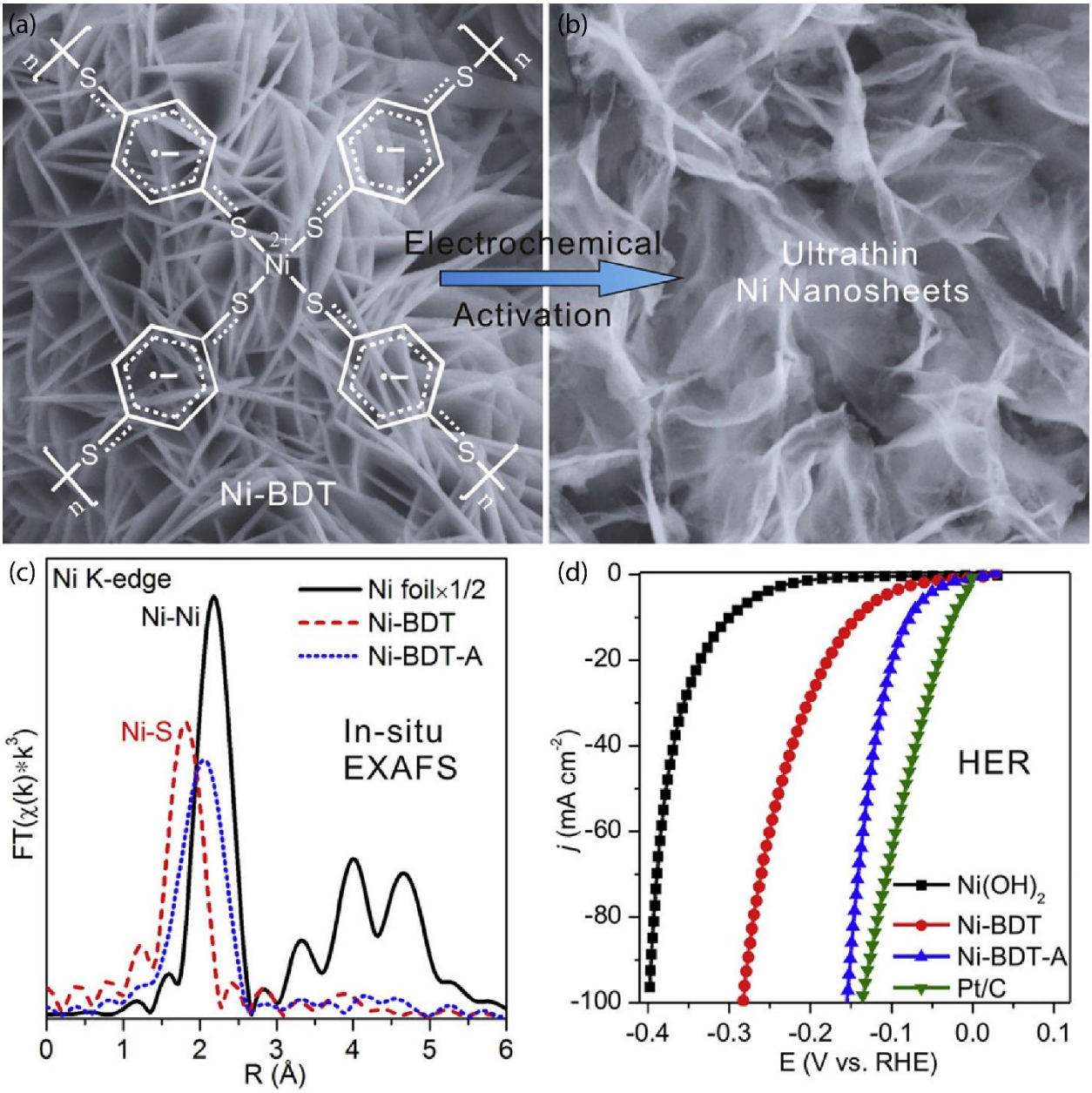

Figure 13. The evolution of Ni-S coordination polymer in electrochemical measurements. (a)(b) the SEM images (a) before and (b) after HER measurements; (c) the EXAFS of reference (Ni foil) and Ni-DBT before and after electrochemical measurements; (d) LSV curves of $Ni(OH)_2$, Ni-BDT, Ni-BDT-A, and Pt/C on a carbon cloth electrode in 1 M KOH (*iR* corrected). Reprinted from Ref.230, copyright 2017, with permission from Cell Press.

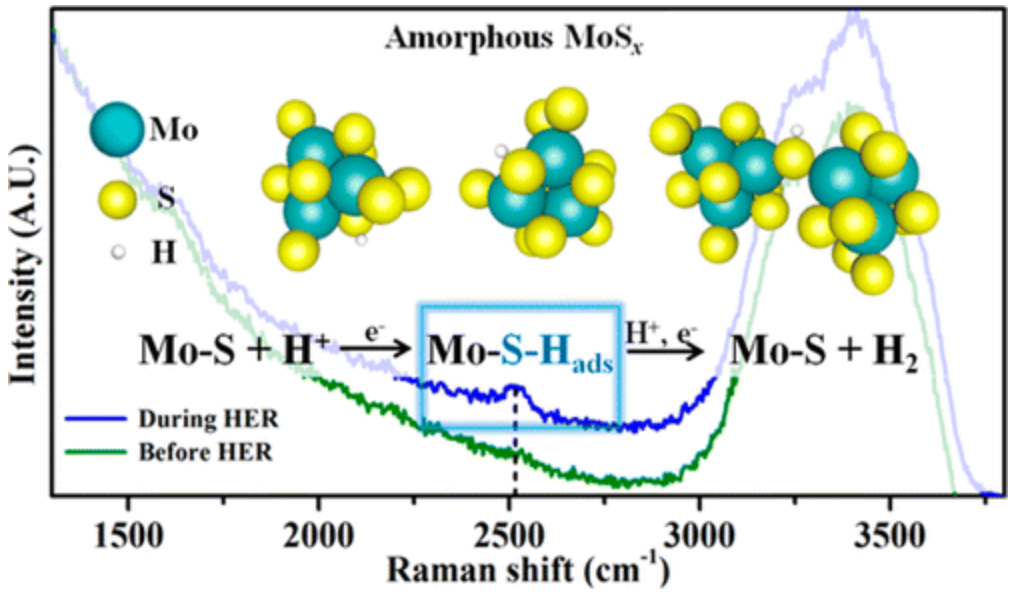

Figure 14. The operando Raman spectroscopy of MoS_x under HER. The peak around 2530 cm^{-1} was assigned to the S-H stretching vibration mode. Reprinted from Ref.46, copyright 2016, with permission from the American Chemistry Society.

4.3. DFT simulation

The discussion of DFT simulation is elaborated from two aspects, the methodology development and the simulation of the electrolyte/electrode interface.

4.3.1. Methodology of DFT

The relative low computation cost and reasonable accuracy for ground state properties, makes DFT outstanding and the most popular amongst all available electronic structure methods. However, the accuracy of exchange-correlation (xc) functional is a recurring issue within the framework of DFT. In particular, there are many xc functionals, all of which vary in accuracy and computational expense. With new xc functionals being developed every year, it can be difficult to stay up-to-date. Here we briefly summarize a few works to offer some perspective.

Commonly, the xc functionals are either constructed from external parameter fitting of large databases ("empirical xc functionals") or from a rigorous theoretical framework with exact constraints ("nonempirical xc functionals"). For example, the revM06-L functional, which was optimized against a vast database with smoothness restraints, yields a mean unsigned error of 3.07 kcal/mol on 422 chemical energies, offering a significant improvement on the previous implementation of M06-L.[11] Another adaptation, is the approach used by Hensley *et al*., wherein they implemented and weighted sum of the energies from RPBE and optB, and found that they were able to yield accurate adsorption energies on transition metal surfaces.[234] On the other hand, these empirically-fitted parameters can be a limitation of these xc functionals as they may rely on unrealistic error cancellation effects, which can be fortuitous. These characteristics limit the generality and predictive power of standard xc functionals which can be highly system dependent. For example, Yungok *et al.* studied the xc functional dependence of H chemisorption thermodynamics with full consideration of binding energies, zero-point energy (ZPE) and vibrational entropy. It was found that the binding energy is the main factor determining the accuracy, but its predictive power is deteriorated by the high variability in the potential energy surface. On the other hand, the vibrational free energy of weakly interacting van der Waals system showed a stronger xc functional dependence. Their discovery highlighted the importance of choosing the correct functional to provide a valid theoretical explanation and prediction.[10, 11, 235, 236]

On the other hand, nonempirical xc functionals were developed by satisfying theoretical constraints and less dependent on specific characteristics of systems. For example, strongly constrained and appropriately normed (SCAN) semi-local density functional was constructed by enforcing 17 known exact constraints that a meta-GGA can.[237] This functional is more accurate

than the GGAs PBE and PBEsol, at nearly the same computational cost. It was shown to give better barrier heights for 76 chemical reactions (BH76 set).[238] However, its application in heterogeneous catalysis such as HER has not been well-validated so far. Other nonempirical xc functional include the Koopmans-compliant hybrid functionals[239-242] and dielectric-dependent hybrid functionals[243-246]. The motivation of these functionals is to well describe dielectric screening of solid-state systems and provide more accurate electronic structure. Therefore, they have been mostly used for predictions of bandgaps, band-alignments instead of reaction energies or barriers.

In addition, advanced theoretical frameworks beyond DFT have been applied to heterogeneous catalysis, which include more accurate electron correlations such as the Random Phase Approximation (RPA), whose exchange treatment is exact and the correlation part is obtained by linear density response function. Per *et al.* employed RPA to compute both the adsorption and surface energies of 10 surface reactions under a low coverage and found that it achieved a high accuracy compared to experimental data while DFT failed to describe either of them accurately (Figure 15).[247] Their study proved that RPA is a better and more universal total energy method for surface science, although it's more computationally demanding. They also employed RPA to calculate the adsorption database of 200 adsorption energies involving OH, CH, NO, CO, N_2, N, O, and H over a wide range of 3d, 4d, and 5d transition metals, which showed a good consistency with a more advanced renormalized adiabatic LDA (rALDA) method, indicating the reliability and generality of RPA for adsorption and surface energy calculations. Another beyond-DFT method for catalysis applications is the multireference method that improves upon the single-particle approach of DFT-based methods. These methods include explicit arrangements of all electrons (*i.e.*, electronic configurations) that are possible within given user-defined spin and

spatial symmetry.[248] While this offers simulations of multi-electron catalysis processes, it is also limited by its greater computational expense.

In summary, regardless of the method chosen, it is clear that serious consideration of the balance between computational accuracy and computational expense must be made in the methodology-benchmarking process. We note community-driven benchmarking can heighten the uniformity and clarify the choice of DFT-based methods.[249]

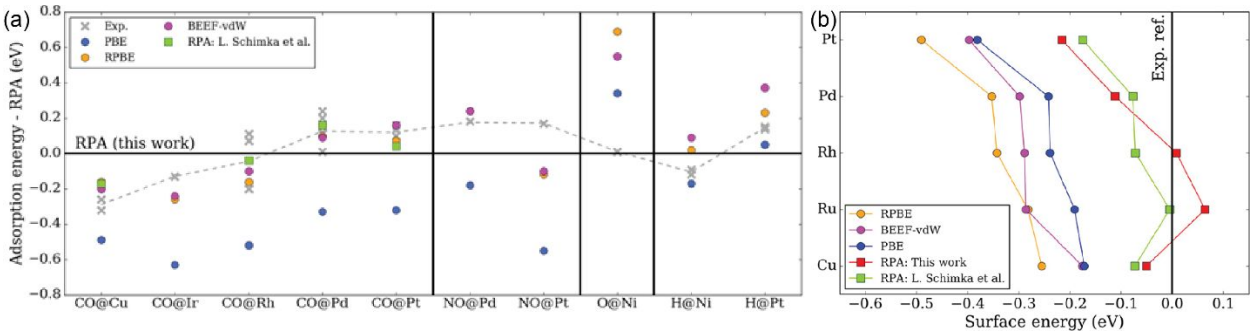

Figure 15. Deviations of adsorption and surface energy between RPA and other methods. Reprinted from Ref.247, copyright 2018, with permission from the American Chemistry Society.

4.3.2. Simulation of the interface between the electrolyte and electrified electrode

The implementation of DFT calculation in electrocatalysis is very challenging since it has to not only describe the electronic structure of the catalyst but also simulate the electrode/electrolyte interface, which poses extra challenges for the implementation of the DFT calculation in electrocatalysis.[48] In this section, the limitations and progress of including the effect of potential, solvent, solute, and pH in the computation will be discussed.

4.3.2.1. Potential

There are two different schemes to include the effect of potential, constant charge scheme and constant potential scheme. For the constant charge scheme, the number of electrons keeps constant, and there is no charge flow in or out of the system. In this scheme, the effect of potential is indirectly included by correcting the energy of electrochemical step (*i.e.* the steps which have electron transfer) by qU, which means potential doesn't have an effect to the energy of chemical step (*i.e.* the steps which don't have electron transfer). However, in reality, even if the step is a chemical step, potential still has an effect on its energy, which is not able to be reflected in the constant charge scheme. While for the constant potential scheme, potential has an effect toward the chemical steps since electrons have to flow in or out of the system to keep the Fermi level fixed, which is closer to the realistic situation.[48] Figure 16 is the reaction pathway of ORR on Pt, which clearly shows the difference between constant charge scheme and constant potential scheme that there is only electron transfer for electrochemical steps in the constant charge scheme, but there is electron transfer for all steps in the constant potential scheme. Wang *et al.* also employed the constant potential scheme to simulate the electric double-layer capacitors and they found that when the potential difference between two electrodes is large such as $\Delta\Psi \geq 4V$, the constant potential scheme showed a significant enhancement over constant charge scheme of "inner-sphere adsorbed" Li^+ ions very close to the electrode surface. The ability of the constant potential scheme being able to respond to the local charge fluctuations in the electrolyte indicates that the constant potential scheme could reduce the energy/barrier for the approaching of Li^+ ions to the electrode surface.[251]

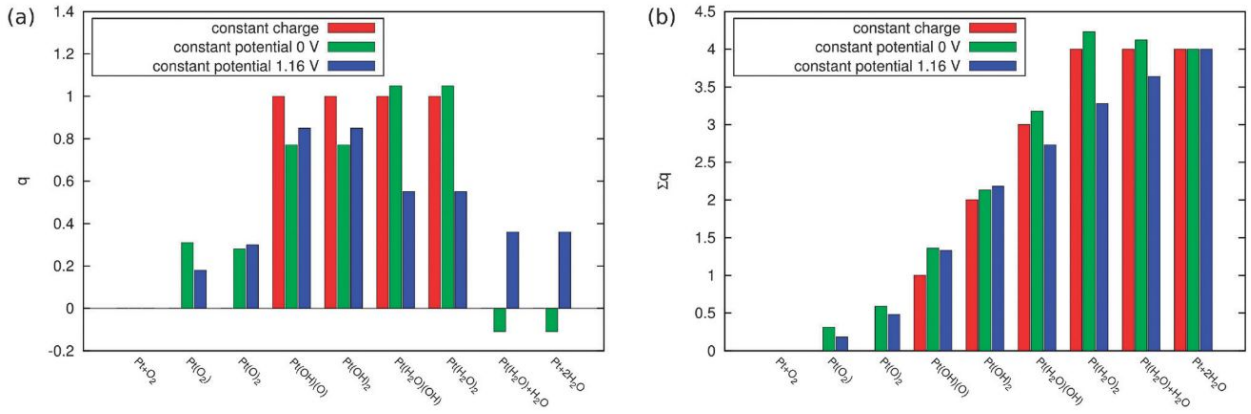

Figure 16. The amount of (a) transferred electrons in each step and (d) cumulative transferred electrons in all steps for the reaction pathway of ORR on Pt calculated by the constant charge and constant potential schemes. Reprinted from Ref.48, copyright 2013, with permission from The Royal Society of Chemistry.

4.3.2.2. Solvent

Since the solvent strongly affects the activity of electrocatalyst, it's necessary to include the effect of the solvent in the DFT calculation. There are two different approaches to simulate the effect of solvent, the explicit solvent model and the implicit solvent model.[252] The explicit solvation model is to include solvent molecules explicitly around the surface of the catalyst, then these solvent molecules will be simulated together with a catalyst to reach thermodynamic equilibrium or compute free energy barriers based on *ab initio* MD as discussed earlier. The explicit solvent model can capture the hydrogen bonds interaction, explicit charge transfer between solvent and catalysts if any, a reasonable ion distribution and physical sampling of solvents.[253] However, the inclusion of huge amounts of solvent molecules required to capture the essential equilibrium properties and statistic averaging substantially increases the computation cost. As a result, implicit solvent models or combined explicit few layers of water molecules with implicit solvent models remain popular.[254] Instead, the implicit solvation model uses a homogeneously

polarizable medium to simulate the effect of solvent molecules. Therefore, it is also called the continuum solvation model.[255] Several parameters need to be included in the construction of implicit solvent models, among which the dielectric constant is the most important because it represents the polarizability of the solvent. Compared to the explicit solvation model, the implicit solvation model can gain the long-range electrostatic effect of the solvent. Its disadvantage is that it cannot include the charge transfer process and physically resolve the local structure of the solvent.

There are two kinds of implicit solvation models, one involves the parametrization based on atomic radii while the other based on solute electron density.[53] For the one based on atomic radii such as the "SM" series and the polarizable continuum models (PCMs),[236, 256, 257] it can be quite accurate for certain systems, but numerical problems which complicate the geometry optimization and MD calculation of the solute would be generated when it is extrapolated to new systems.[53] On the other hand, for the solute electron density based implicit solvation model such as the self-consistent continuum solvation (SCCS) approach,[258, 259] it uses a varying dielectric constant determined from the solute electron density, which avoids the numerical issues in atomic radii based models. Besides, the density-based models require fewer parameters for the fitting, which makes it more reliable to extrapolate from one system to another system. However, the fewer parameters of density-based models also make them less accurate compared to the atomic radii-based models. Especially for those charge asymmetric systems, the density based models over-solvate cations and under-solvate anions.[53] Sundararaman *et al.* developed a density-based implicit solvation model, which is able to handle the aforementioned charge asymmetric problem by including the cavity dependence on the solute electron density and potential. This new model is based on the charge-asymmetric nonlocally determined local electric response, referred to as the CANDLE solvation model.[53] As shown in Figure 17, the CANDLE model shows a much better

consistency with the experimental results compared to the linear PCM method, and can reproduce solvation energies of neutral molecules, cation and anions with only a mean absolute error of 1.8 kcal mol^{-1} in water and 3.0 kcal mol^{-1} in acetonitrile.

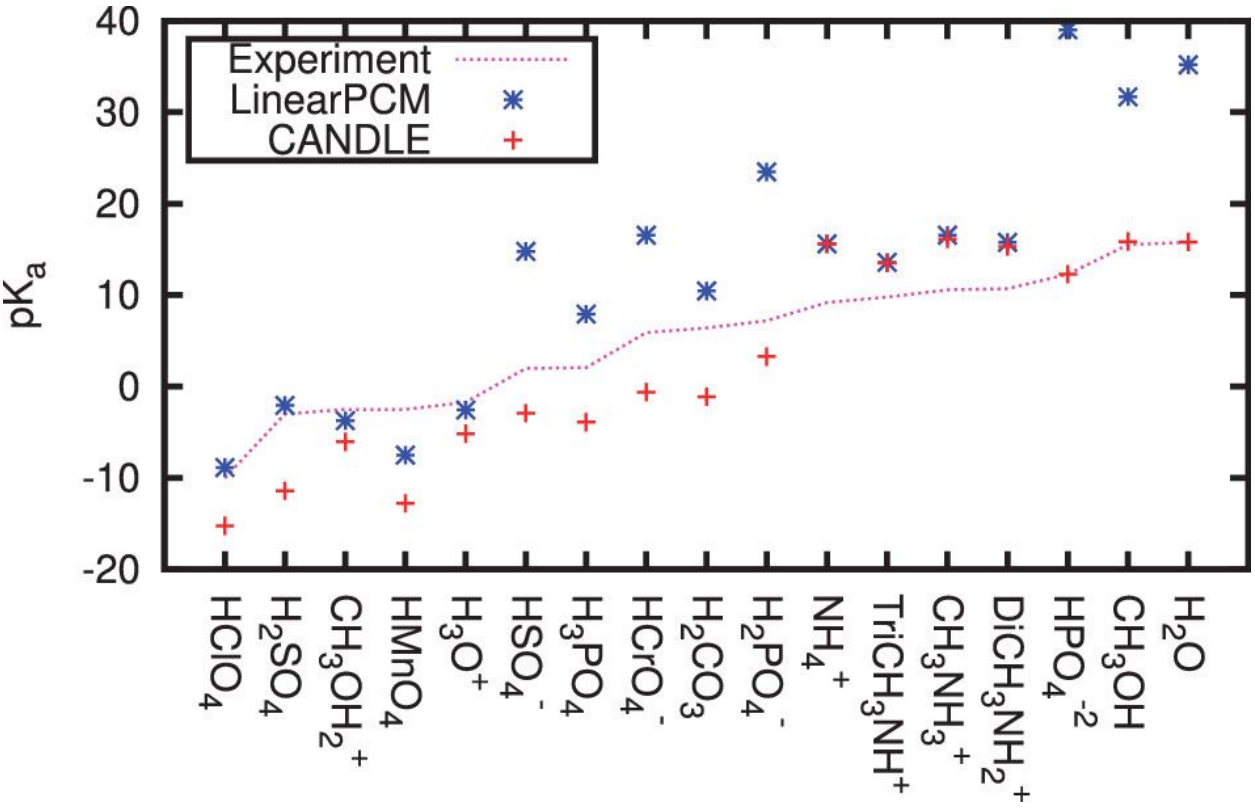

Figure 17. Acid dissociation constant (pK_a) of different molecules and ions in H_2O predicted by the CANDLE model and linear PCM method compared to that of the experiment. Reprinted from Ref.53, copyright 2015, with permission from the American Institute of Physics.

4.3.2.3. Solute

Solute strongly affects the activity of electrocatalyst, which has already been verified experimentally and theoretically. For example, Shinagawa *et al.* studied the effect of solute concentration on ORR and HOR on Pt in a buffered solution.[260] It was found that the higher

concentration of solute decreased the gas solubility, increased the kinematic viscosity of the solution and the diffusion coefficient of the dissolved gas. Pham *et al.* studied the electronic structure of aqueous liquid by a combination of first principles methods, experimental verification, and spectroscopic measurements.[54] By using a dielectric hybrid functional, range-separated hybrid (RSH) and self-consistent hybrid (sc-hybrid) functionals, the ionization potentials (IPs) of 16 solvated anions can be accurately captured and were comparable to the experimental data. Besides, the proposed computational framework can also be applied to other liquids, which proved the generality of the method and paved the way for understanding and engineering the electrolyte for different energy conversion and storage techniques.

4.3.2.4. pH

The activity of electrocatalyst strongly depends on the pH of electrolyte. A good example is that the HER activity of Pt in alkaline medium is two to three orders lower than that in acidic medium.[83] One approach to simulate the effect of pH is to convert the pH effect to potential effect. For example, Cheng *et al.* studied the pH dependence of H binding energy on Pt(100)/H_2O and a pH change from 0.2 to 12.8 at U = +0.3 V (vs RHE) was converted to the potential change from +0.29 to −0.46 V on SHE scale by Nernst equation.[32] However, this conversion is only applicable for surfaces on which H^+ and OH^- are the only charge determining ions.[261-263] Another approach to simulate the effect of pH is to correlate pH at the point of zero charge (pH_{ZPC}) with the chemical potential of an isolated proton. Ambrosio *et al.* used this method to study the pH dependence surface chemistry over $BiVO_4$ (010)-water interface by supplementing electronic structure calculation, MD calculation, and thermodynamic integration method together.[55] A pH dependence diagram of $BiVO_4$ (010) surface in an aqueous environment was plotted via the h-rVV10 level of

theory, finding that protons, H_2O molecules, and hydroxide ions are the dominant adsorbates under strong acidic condition, pH ranging from 2 to 8, and pH larger than 8.2, respectively (Figure 18).

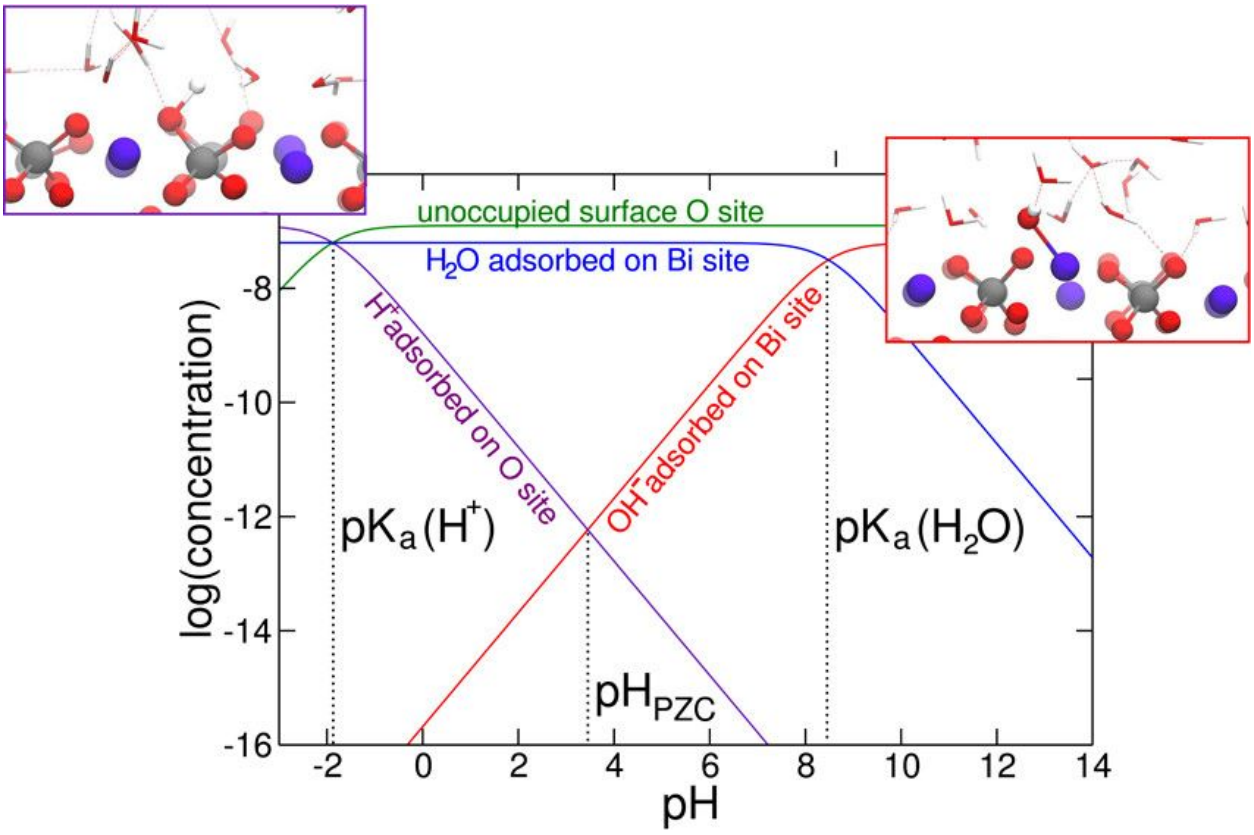

Figure 18. The pH-dependent surface chemistry of the $BiVO_4$(010)-water interface. Reprinted from Ref.55, copyright 2018, with permission from American Chemical Society.

5. Summary and outlooks

Integrating experimental and computational efforts has been proven to be highly effective in moving forward to the field of electrocatalysis. In this article, we have reviewed the recent accomplishments, developments, and limitations in implementing DFT for studying HER catalysts. Here we would like to share some suggestions in the coupling of experiments and DFT calculation (Figure 19). First, in order to improve consistency between experimental and simulation results,

the catalytic system has to be well-defined and it should be as simple as possible. A complicated structure consisted of different phases and defects would create too many possibilities and rapidly increase the computational cost. A single crystal system would be preferred from a computational perspective. Second, experimental measurements should be carefully performed, for example, using steady current instead of the current obtained from LSV, minimizing mass diffusion limitation via rotating the electrodes and/or using ordered porous structures, and accurately measuring the ECSA for determining accurate intrinsic activities. Third, it is important to use the correct and accurate structural information to build DFT model. *Operando* techniques are highly preferred in probing the structural information of the catalyst under the working environment.[162] If *in-situ* measurements are impossible, then structural information of the catalyst should be collected at least before and after the electrochemical measurements to verify any possible structural changes during the reaction. Surface Pourbaix diagram is recommended to be calculated given the thermodynamic most stable phase and surface termination varies under different pH and potential.[157] Finally, to perform DFT calculation closer to the real working condition, xc functionals have to be carefully chosen. In certain cases, it is recommended to use higher level total energy calculation method such as RPA, to compute desired quantities. Furthermore, correctly and accurately simulating the interface between the electrolyte and electrified electrode is critical for understanding the catalytic reactions. Factors, including potential, solute, solvent and pH, should be carefully considered. Although numerous methods have been developed to simulate these effects, each method has its limitations. For example, the implicit solvation model is not able to capture the charge transfer process and physically resolve the local structure of the solvent. Therefore, new methods have to be developed to tackle these issues. We believe that the seamless coupling between experiments and DFT calculation can deepen the understanding of catalytic

mechanisms of different catalysts, and accelerate the development of new electrocatalysts for different reactions and conditions.

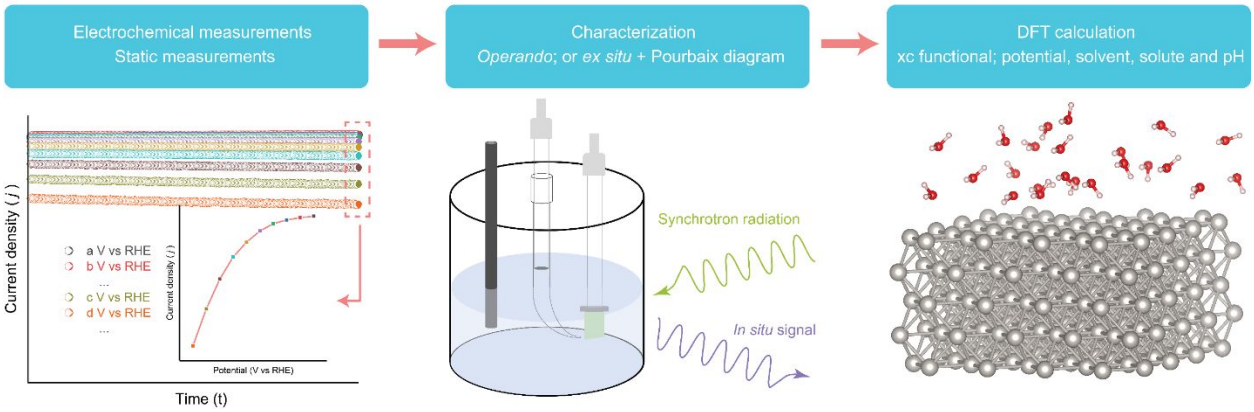

Figure 19. A schematic illustration of coupling experiments with DFT calculation.

Conflicts of interest

There are no conflicts of interest to declare.

Acknowledgments

Y.P. acknowledges the support of the National Science Foundation under Grants No. DMR-1760260 and No. CHE-1904547. Y.L. acknowledge the financial support from Merced nAnomaterials Center for Energy and Sensing (MACES), a NASA funded MIRO center, under award NNX15AQ01.

References

1. L. Barreto, A. Makihira and K. Riahi, *International Journal of Hydrogen Energy*, 2003, **28**, 267-284.
2. F. Mueller-Langer, E. Tzimas, M. Kaltschmitt and S. Peteves, *International Journal of Hydrogen Energy*, 2007, **32**, 3797-3810.
3. R. Ramachandran and R. K. Menon, *International Journal of Hydrogen Energy*, 1998, **23**, 593-598.
4. W. C. Lattin and V. P. Utgikar, *International Journal of Hydrogen Energy*, 2007, **32**, 3230-3237.
5. M. Z. Jacobson, W. G. Colella and D. M. Golden, *Science*, 2005, **308**, 1901.
6. D. L. Trimm and Z. I. Önsan, *Catalysis Reviews*, 2001, **43**, 31-84.
7. J. M. Ogden, *Annual Review of Energy and the Environment*, 1999, **24**, 227-279.
8. S. Satyapal, J. Petrovic, C. Read, G. Thomas and G. Ordaz, *Catalysis Today*, 2007, **120**, 246-256.
9. Z. W. Seh, J. Kibsgaard, C. F. Dickens, I. Chorkendorff, J. K. Nørskov and T. F. Jaramillo, *Science*, 2017, **355**, eaad4998.
10. Y. Zhao and D. G. Truhlar, *Journal of Chemical Theory and Computation*, 2011, **7**, 669-676.
11. Y. Wang, X. Jin, H. S. Yu, D. G. Truhlar and X. He, *Proceedings of the National Academy of Sciences*, 2017, **114**, 8487.
12. P. J. Hasnip, K. Refson, M. I. J. Probert, J. R. Yates, S. J. Clark and C. J. Pickard, *Philosophical Transactions of the Royal Society A: Mathematical, Physical and Engineering Sciences*, 2014, **372**, 20130270.
13. N. Mardirossian and M. Head-Gordon, *Molecular Physics*, 2017, **115**, 2315-2372.
14. B. Hammer, L. B. Hansen and J. K. Nørskov, *Physical Review B*, 1999, **59**, 7413-7421.
15. J. K. Nørskov, F. Abild-Pedersen, F. Studt and T. Bligaard, *Proceedings of the National Academy of Sciences*, 2011, **108**, 937.
16. T. list, 2019.
17. D. R. Bowler, J. S. Baker, J. T. L. Poulton, S. Y. Mujahed, J. Lin, S. Yadav, Z. Raza and T. Miyazaki, *Japanese Journal of Applied Physics*, 2019, **58**, 100503.
18. A. Erba, J. Baima, I. Bush, R. Orlando and R. Dovesi, *Journal of Chemical Theory and Computation*, 2017, **13**, 5019-5027.
19. W. Hu, L. Lin and C. Yang, *The Journal of Chemical Physics*, 2015, **143**, 124110.
20. S. Niu, Y. Fang, J. Zhou, J. Cai, Y. Zang, Y. Wu, J. Ye, Y. Xie, Y. Liu, X. Zheng, W. Qu, X. Liu, G. Wang and Y. Qian, *Journal of Materials Chemistry A*, 2019, **7**, 10924-10929.
21. S. Liu, C. Chen, Y. Zhang, Q. Zheng, S. Zhang, X. Mu, C. Chen, J. Ma and S. Mu, *Journal of Materials Chemistry A*, 2019, **7**, 14466-14472.
22. M. Mavrikakis, B. Hammer and J. K. Nørskov, *Physical Review Letters*, 1998, **81**, 2819-2822.

23. Y. Zang, S. Niu, Y. Wu, X. Zheng, J. Cai, J. Ye, Y. Xie, Y. Liu, J. Zhou, J. Zhu, X. Liu, G. Wang and Y. Qian, *Nature Communications*, 2019, **10**, 1217.
24. R. Subbaraman, D. Tripkovic, D. Strmcnik, K.-C. Chang, M. Uchimura, A. P. Paulikas, V. Stamenkovic and N. M. Markovic, *Science*, 2011, **334**, 1256.
25. Y. Zheng, Y. Jiao, A. Vasileff and S.-Z. Qiao, *Angewandte Chemie International Edition*, 2018, **57**, 7568-7579.
26. D. Wang, X. Zhang, S. Bao, Z. Zhang, H. Fei and Z. Wu, *Journal of Materials Chemistry A*, 2017, **5**, 2681-2688.
27. D. Malevich, E. Halliop, B. A. Peppley, J. G. Pharoah and K. Karan, *Journal of The Electrochemical Society*, 2009, **156**, B216-B224.
28. Z. Lu, W. Zhu, X. Yu, H. Zhang, Y. Li, X. Sun, X. Wang, H. Wang, J. Wang, J. Luo, X. Lei and L. Jiang, *Advanced Materials*, 2014, **26**, 2683-2687.
29. J. Hao, W. Yang, Z. Huang and C. Zhang, *Advanced Materials Interfaces*, 2016, **3**, 1600236.
30. J. C. Meier, C. Galeano, I. Katsounaros, A. A. Topalov, A. Kostka, F. Schüth and K. J. J. Mayrhofer, *ACS Catalysis*, 2012, **2**, 832-843.
31. J. C. Meier, I. Katsounaros, C. Galeano, H. J. Bongard, A. A. Topalov, A. Kostka, A. Karschin, F. Schüth and K. J. J. Mayrhofer, *Energy & Environmental Science*, 2012, **5**, 9319-9330.
32. T. Cheng, L. Wang, B. V. Merinov and W. A. Goddard, *Journal of the American Chemical Society*, 2018, **140**, 7787-7790.
33. Q. Tang and D.-e. Jiang, *ACS Catalysis*, 2016, **6**, 4953-4961.
34. Y. Huang, R. J. Nielsen and W. A. Goddard, *Journal of the American Chemical Society*, 2018, **140**, 16773-16782.
35. Y. Huang, R. J. Nielsen, W. A. Goddard and M. P. Soriaga, *Journal of the American Chemical Society*, 2015, **137**, 6692-6698.
36. B. Hinnemann, P. G. Moses, J. Bonde, K. P. Jørgensen, J. H. Nielsen, S. Horch, I. Chorkendorff and J. K. Nørskov, *Journal of the American Chemical Society*, 2005, **127**, 5308-5309.
37. Y. Zheng, Y. Jiao, Y. Zhu, L. H. Li, Y. Han, Y. Chen, A. Du, M. Jaroniec and S. Z. Qiao, *Nature Communications*, 2014, **5**, 3783.
38. B. Qiao, A. Wang, X. Yang, L. F. Allard, Z. Jiang, Y. Cui, J. Liu, J. Li and T. Zhang, *Nature Chemistry*, 2011, **3**, 634.
39. Z. W. Seh, K. D. Fredrickson, B. Anasori, J. Kibsgaard, A. L. Strickler, M. R. Lukatskaya, Y. Gogotsi, T. F. Jaramillo and A. Vojvodic, *ACS Energy Letters*, 2016, **1**, 589-594.
40. M. A. Lukowski, A. S. Daniel, F. Meng, A. Forticaux, L. Li and S. Jin, *Journal of the American Chemical Society*, 2013, **135**, 10274-10277.
41. H. Li, C. Tsai, A. L. Koh, L. Cai, A. W. Contryman, A. H. Fragapane, J. Zhao, H. S. Han, H. C. Manoharan, F. Abild-Pedersen, J. K. Nørskov and X. Zheng, *Nature Materials*, 2016, **15**, 48-53.
42. T. F. Jaramillo, K. P. Jørgensen, J. Bonde, J. H. Nielsen, S. Horch and I. Chorkendorff, *Science*, 2007, **317**, 100.
43. C. Choi, S. Back, N.-Y. Kim, J. Lim, Y.-H. Kim and Y. Jung, *ACS Catalysis*, 2018, **8**, 7517-7525.
44. G. Gao, A. P. O'Mullane and A. Du, *ACS Catalysis*, 2017, **7**, 494-500.

45. C. Wei, S. Sun, D. Mandler, X. Wang, S. Z. Qiao and Z. J. Xu, *Chemical Society Reviews*, 2019, **48**, 2518-2534.
46. Y. Deng, L. R. L. Ting, P. H. L. Neo, Y.-J. Zhang, A. A. Peterson and B. S. Yeo, *ACS Catalysis*, 2016, **6**, 7790-7798.
47. V. I. Anisimov, J. Zaanen and O. K. Andersen, *Physical Review B*, 1991, **44**, 943-954.
48. U. Benedikt, W. B. Schneider and A. A. Auer, *Physical Chemistry Chemical Physics*, 2013, **15**, 2712-2724.
49. Y. Ping, R. J. Nielsen and W. A. Goddard, *Journal of the American Chemical Society*, 2017, **139**, 149-155.
50. T. Cheng, H. Xiao and W. A. Goddard, *Proceedings of the National Academy of Sciences*, 2017, **114**, 1795.
51. T. Cheng, H. Xiao and W. A. Goddard, *Journal of the American Chemical Society*, 2016, **138**, 13802-13805.
52. H. Xiao, T. Cheng and W. A. Goddard, *Journal of the American Chemical Society*, 2017, **139**, 130-136.
53. R. Sundararaman and W. A. Goddard, *The Journal of Chemical Physics*, 2015, **142**, 064107.
54. T. A. Pham, M. Govoni, R. Seidel, S. E. Bradforth, E. Schwegler and G. Galli, *Science Advances*, 2017, **3**, e1603210.
55. F. Ambrosio, J. Wiktor and A. Pasquarello, *ACS Applied Materials & Interfaces*, 2018, **10**, 10011-10021.
56. D. Kong, H. Wang, J. J. Cha, M. Pasta, K. J. Koski, J. Yao and Y. Cui, *Nano Letters*, 2013, **13**, 1341-1347.
57. J. Kibsgaard, Z. Chen, B. N. Reinecke and T. F. Jaramillo, *Nature Materials*, 2012, **11**, 963-969.
58. Y. Wu, X. Liu, D. Han, X. Song, L. Shi, Y. Song, S. Niu, Y. Xie, J. Cai, S. Wu, J. Kang, J. Zhou, Z. Chen, X. Zheng, X. Xiao and G. Wang, *Nature Communications*, 2018, **9**, 1425.
59. H. Wang, X.-B. Li, L. Gao, H.-L. Wu, J. Yang, L. Cai, T.-B. Ma, C.-H. Tung, L.-Z. Wu and G. Yu, *Angewandte Chemie International Edition*, 2018, **57**, 192-197.
60. T. Kou, M. Chen, F. Wu, T. J. Smart, S. Wang, Y. Wu, Y. Zhang, S. Li, S. Lall, Z. Zhang, Y.-S. Liu, J. Guo, G. Wang, Y. Ping and Y. Li, *Nature Communications*, 2020, **11**, 590.
61. X. Zou and Y. Zhang, *Chemical Society Reviews*, 2015, **44**, 5148-5180.
62. M. R. G. de Chialvo and A. C. Chialvo, *Journal of Electroanalytical Chemistry*, 1994, **372**, 209-223.
63. M. R. Gennero de Chialvo and A. C. Chialvo, *Electrochimica Acta*, 1998, **44**, 841-851.
64. K. Zeng and D. Zhang, *Progress in Energy and Combustion Science*, 2010, **36**, 307-326.
65. J. Greeley, T. F. Jaramillo, J. Bonde, I. Chorkendorff and J. K. Nørskov, *Nature Materials*, 2006, **5**, 909-913.
66. Q. Zhang, D. Q. Lima, I. Lee, F. Zaera, M. Chi and Y. Yin, *Angewandte Chemie International Edition*, 2011, **50**, 7088-7092.

67. H. Wang, C. Tsai, D. Kong, K. Chan, F. Abild-Pedersen, J. K. Nørskov and Y. Cui, *Nano Research*, 2015, **8**, 566-575.
68. D.-Y. Wang, M. Gong, H.-L. Chou, C.-J. Pan, H.-A. Chen, Y. Wu, M.-C. Lin, M. Guan, J. Yang, C.-W. Chen, Y.-L. Wang, B.-J. Hwang, C.-C. Chen and H. Dai, *Journal of the American Chemical Society*, 2015, **137**, 1587-1592.
69. T. Kou, T. Smart, B. Yao, I. Chen, D. Thota, Y. Ping and Y. Li, *Advanced Energy Materials*, 2018, **8**, 1703538.
70. P. Raybaud, J. Hafner, G. Kresse, S. Kasztelan and H. Toulhoat, *Journal of Catalysis*, 2000, **189**, 129-146.
71. T. Zheng, W. Sang, Z. He, Q. Wei, B. Chen, H. Li, C. Cao, R. Huang, X. Yan, B. Pan, S. Zhou and J. Zeng, *Nano Letters*, 2017, **17**, 7968-7973.
72. J. R. Kitchin, J. K. Nørskov, M. A. Barteau and J. G. Chen, *Physical Review Letters*, 2004, **93**, 156801.
73. M. Luo and S. Guo, *Nature Reviews Materials*, 2017, **2**, 17059.
74. D. Voiry, H. Yamaguchi, J. Li, R. Silva, D. C. B. Alves, T. Fujita, M. Chen, T. Asefa, V. B. Shenoy, G. Eda and M. Chhowalla, *Nature Materials*, 2013, **12**, 850-855.
75. B. Hammer and J. K. Norskov, *Nature*, 1995, **376**, 238-240.
76. J. Greeley, J. K. Nørskov and M. Mavrikakis, *Annual Review of Physical Chemistry*, 2002, **53**, 319-348.
77. K. Sakmann, A. I. Streltsov, O. E. Alon and L. S. Cederbaum, *Physical Review Letters*, 2009, **103**, 220601.
78. K. Yan, T. A. Maark, A. Khorshidi, V. A. Sethuraman, A. A. Peterson and P. R. Guduru, *Angewandte Chemie International Edition*, 2016, **55**, 6175-6181.
79. Y. Jiao, Y. Zheng, M. Jaroniec and S. Z. Qiao, *Chemical Society Reviews*, 2015, **44**, 2060-2086.
80. A. Vojvodic, A. Hellman, C. Ruberto and B. I. Lundqvist, *Physical Review Letters*, 2009, **103**, 146103.
81. Z. Li, J.-Y. Fu, Y. Feng, C.-K. Dong, H. Liu and X.-W. Du, *Nature Catalysis*, 2019, DOI: 10.1038/s41929-019-0365-9.
82. L. Wang, Z. Zeng, W. Gao, T. Maxson, D. Raciti, M. Giroux, X. Pan, C. Wang and J. Greeley, *Science*, 2019, **363**, 870.
83. W. Sheng, H. A. Gasteiger and Y. Shao-Horn, *Journal of The Electrochemical Society*, 2010, **157**, B1529-B1536.
84. R. Subbaraman, D. Tripkovic, K.-C. Chang, D. Strmcnik, A. P. Paulikas, P. Hirunsit, M. Chan, J. Greeley, V. Stamenkovic and N. M. Markovic, *Nature Materials*, 2012, **11**, 550-557.
85. D. Strmcnik, M. Uchimura, C. Wang, R. Subbaraman, N. Danilovic, D. van der Vliet, A. P. Paulikas, V. R. Stamenkovic and N. M. Markovic, *Nature Chemistry*, 2013, **5**, 300-306.
86. J. Zheng, W. Sheng, Z. Zhuang, B. Xu and Y. Yan, *Science Advances*, 2016, **2**, e1501602.
87. E. Liu, J. Li, L. Jiao, H. T. T. Doan, Z. Liu, Z. Zhao, Y. Huang, K. M. Abraham, S. Mukerjee and Q. Jia, *Journal of the American Chemical Society*, 2019, **141**, 3232-3239.
88. N. Ramaswamy, S. Ghoshal, M. K. Bates, Q. Jia, J. Li and S. Mukerjee, *Nano Energy*, 2017, **41**, 765-771.

89. S. Intikhab, J. D. Snyder and M. H. Tang, *ACS Catalysis*, 2017, **7**, 8314-8319.
90. B. L. Trout and M. Parrinello, *The Journal of Physical Chemistry B*, 1999, **103**, 7340-7345.
91. Y.-C. Hao, Y. Guo, L.-W. Chen, M. Shu, X.-Y. Wang, T.-A. Bu, W.-Y. Gao, N. Zhang, X. Su, X. Feng, J.-W. Zhou, B. Wang, C.-W. Hu, A.-X. Yin, R. Si, Y.-W. Zhang and C.-H. Yan, *Nature Catalysis*, 2019, **2**, 448-456.
92. G. Henkelman and H. Jónsson, *The Journal of Chemical Physics*, 2000, **113**, 9978-9985.
93. G. Henkelman, B. P. Uberuaga and H. Jónsson, *The Journal of Chemical Physics*, 2000, **113**, 9901-9904.
94. P. Xiao, D. Sheppard, J. Rogal and G. Henkelman, *The Journal of Chemical Physics*, 2014, **140**, 174104.
95. K. Tianyi, C. M. Chen, W. Feng, S. T. J, W. Shanwen, W. Yishang, Z. Ying, L. Shengtong, L. Supriya, Z. Zhonghua, L. Yi-Sheng, G. J. Guo, W. Gongming, P. Yuan and L. Yat, *Nature Communications*, 2020, DOI: 10.1038/s41467-020-14462-2.
96. J. Hu, C. Zhang, L. Jiang, H. Lin, Y. An, D. Zhou, M. K. H. Leung and S. Yang, *Joule*, 2017, **1**, 383-393.
97. Y. Xie, J. Cai, Y. Wu, Y. Zang, X. Zheng, J. Ye, P. Cui, S. Niu, Y. Liu, J. Zhu, X. Liu, G. Wang and Y. Qian, *Advanced Materials*, 2019, **31**, 1807780.
98. Z. Lu, W. Xu, W. Zhu, Q. Yang, X. Lei, J. Liu, Y. Li, X. Sun and X. Duan, *Chemical Communications*, 2014, **50**, 6479-6482.
99. T. Kou, S. Wang, J. L. Hauser, M. Chen, S. R. J. Oliver, Y. Ye, J. Guo and Y. Li, *ACS Energy Letters*, 2019, **4**, 622-628.
100. X. Yu, J. Zhao, L.-R. Zheng, Y. Tong, M. Zhang, G. Xu, C. Li, J. Ma and G. Shi, *ACS Energy Letters*, 2018, **3**, 237-244.
101. H. Jiang, Y. Lin, B. Chen, Y. Zhang, H. Liu, X. Duan, D. Chen and L. Song, *Materials Today*, 2018, **21**, 602-610.
102. M. Sheng, B. Jiang, B. Wu, F. Liao, X. Fan, H. Lin, Y. Li, Y. Lifshitz, S.-T. Lee and M. Shao, *ACS Nano*, 2019, **13**, 2786-2794.
103. C.-T. Dinh, A. Jain, F. P. G. de Arquer, P. De Luna, J. Li, N. Wang, X. Zheng, J. Cai, B. Z. Gregory, O. Voznyy, B. Zhang, M. Liu, D. Sinton, E. J. Crumlin and E. H. Sargent, *Nature Energy*, 2019, **4**, 107-114.
104. M. G. Evans and M. Polanyi, *Transactions of the Faraday Society*, 1938, **34**, 11-24.
105. R. P. Bell and C. N. Hinshelwood, *Proceedings of the Royal Society of London. Series A - Mathematical and Physical Sciences*, 1936, **154**, 414-429.
106. T. Bligaard, J. K. Nørskov, S. Dahl, J. Matthiesen, C. H. Christensen and J. Sehested, *Journal of Catalysis*, 2004, **224**, 206-217.
107. Y. Li, H. Wang, L. Xie, Y. Liang, G. Hong and H. Dai, *Journal of the American Chemical Society*, 2011, **133**, 7296-7299.
108. Y. Gong, L. Wang, H. Xiong, M. Shao, L. Xu, A. Xie, S. Zhuang, Y. Tang, X. Yang, Y. Chen and P. Wan, *Journal of Materials Chemistry A*, 2019, **7**, 13671-13678.
109. K. Xiong, L. Li, L. Zhang, W. Ding, L. Peng, Y. Wang, S. Chen, S. Tan and Z. Wei, *Journal of Materials Chemistry A*, 2015, **3**, 1863-1867.

110. D. Voiry, R. Fullon, J. Yang, C. de Carvalho Castro e Silva, R. Kappera, I. Bozkurt, D. Kaplan, M. J. Lagos, P. E. Batson, G. Gupta, Aditya D. Mohite, L. Dong, D. Er, V. B. Shenoy, T. Asefa and M. Chhowalla, *Nature Materials*, 2016, **15**, 1003-1009.
111. Y. Wang, L. Liu, X. Zhang, F. Yan, C. Zhu and Y. Chen, *Journal of Materials Chemistry A*, 2019, **7**, 22412-22419.
112. R. Patil, V. Juvekar and U. Nalage, 2017.
113. D. Kiuchi, H. Matsushima, Y. Fukunaka and K. Kuribayashi, *Journal of The Electrochemical Society*, 2006, **153**, E138-E143.
114. M. Wang, Z. Wang, X. Gong and Z. Guo, *Renewable and Sustainable Energy Reviews*, 2014, **29**, 573-588.
115. K. Qian, Z. D. Chen and J. J. J. Chen, *Journal of Applied Electrochemistry*, 1998, **28**, 1141-1145.
116. S. Geiger, O. Kasian, M. Ledendecker, E. Pizzutilo, A. M. Mingers, W. T. Fu, O. Diaz-Morales, Z. Li, T. Oellers, L. Fruchter, A. Ludwig, K. J. J. Mayrhofer, M. T. M. Koper and S. Cherevko, *Nature Catalysis*, 2018, **1**, 508-515.
117. N. Artrith and A. M. Kolpak, *Computational Materials Science*, 2015, **110**, 20-28.
118. K. J. J. Mayrhofer, S. J. Ashton, J. C. Meier, G. K. H. Wiberg, M. Hanzlik and M. Arenz, *Journal of Power Sources*, 2008, **185**, 734-739.
119. K. J. J. Mayrhofer, J. C. Meier, S. J. Ashton, G. K. H. Wiberg, F. Kraus, M. Hanzlik and M. Arenz, *Electrochemistry Communications*, 2008, **10**, 1144-1147.
120. M. J. N. Pourbaix, 1974, **307**.
121. F. J. Perez-Alonso, C. F. Elkjær, S. S. Shim, B. L. Abrams, I. E. Stephens and I. J. J. o. P. S. Chorkendorff, 2011, **196**, 6085-6091.
122. K. Schlögl, K. J. J. Mayrhofer, M. Hanzlik and M. Arenz, *Journal of Electroanalytical Chemistry*, 2011, **662**, 355-360.
123. Y. Shao-Horn, W. C. Sheng, S. Chen, P. J. Ferreira, E. F. Holby and D. Morgan, *Topics in Catalysis*, 2007, **46**, 285-305.
124. K. Hartl, M. Hanzlik and M. Arenz, *Energy & Environmental Science*, 2011, **4**, 234-238.
125. H. Schulenburg, B. Schwanitz, N. Linse, G. G. Scherer, A. Wokaun, J. Krbanjevic, R. Grothausmann and I. Manke, *The Journal of Physical Chemistry C*, 2011, **115**, 14236-14243.
126. M. M. Mench, E. C. Kumbur and T. N. Veziroglu, *Polymer electrolyte fuel cell degradation*, Academic Press, 2011.
127. M. Ma, K. Liu, J. Shen, R. Kas and W. A. Smith, *ACS Energy Letters*, 2018, **3**, 1301-1306.
128. K. Hu, T. Ohto, L. Chen, J. Han, M. Wakisaka, Y. Nagata, J.-i. Fujita and Y. Ito, *ACS Energy Letters*, 2018, **3**, 1539-1544.
129. M. Ledendecker, J. S. Mondschein, O. Kasian, S. Geiger, D. Göhl, M. Schalenbach, A. Zeradjanin, S. Cherevko, R. E. Schaak and K. Mayrhofer, *Angewandte Chemie International Edition*, 2017, **56**, 9767-9771.
130. J. Bonde, P. G. Moses, T. F. Jaramillo, J. K. Nørskov and I. Chorkendorff, *Faraday Discussions*, 2009, **140**, 219-231.
131. D. Voiry, M. Salehi, R. Silva, T. Fujita, M. Chen, T. Asefa, V. B. Shenoy, G. Eda and M. Chhowalla, *Nano Letters*, 2013, **13**, 6222-6227.

132. C. Tsai, H. Li, S. Park, J. Park, H. S. Han, J. K. Nørskov, X. Zheng and F. Abild-Pedersen, *Nature Communications*, 2017, **8**, 15113.
133. J. Hong, Z. Hu, M. Probert, K. Li, D. Lv, X. Yang, L. Gu, N. Mao, Q. Feng, L. Xie, J. Zhang, D. Wu, Z. Zhang, C. Jin, W. Ji, X. Zhang, J. Yuan and Z. Zhang, *Nature Communications*, 2015, **6**, 6293.
134. C. G. Morales-Guio and X. Hu, *Accounts of Chemical Research*, 2014, **47**, 2671-2681.
135. H. Vrubel and X. Hu, *ACS Catalysis*, 2013, **3**, 2002-2011.
136. D. Merki, S. Fierro, H. Vrubel and X. Hu, *Chemical Science*, 2011, **2**, 1262-1267.
137. Y. Zheng, Y. Jiao, L. H. Li, T. Xing, Y. Chen, M. Jaroniec and S. Z. Qiao, *ACS Nano*, 2014, **8**, 5290-5296.
138. C. Hu and L. Dai, *Advanced Materials*, 2017, **29**, 1604942.
139. L. Zhang, J. Xiao, H. Wang and M. Shao, *ACS Catalysis*, 2017, **7**, 7855-7865.
140. Y. Jiao, Y. Zheng, K. Davey and S.-Z. Qiao, *Nature Energy*, 2016, **1**, 16130.
141. N. Cheng, S. Stambula, D. Wang, M. N. Banis, J. Liu, A. Riese, B. Xiao, R. Li, T.-K. Sham, L.-M. Liu, G. A. Botton and X. Sun, *Nature Communications*, 2016, **7**, 13638.
142. J. Deng, H. Li, J. Xiao, Y. Tu, D. Deng, H. Yang, H. Tian, J. Li, P. Ren and X. Bao, *Energy & Environmental Science*, 2015, **8**, 1594-1601.
143. K. Jiang, B. Liu, M. Luo, S. Ning, M. Peng, Y. Zhao, Y.-R. Lu, T.-S. Chan, F. M. F. de Groot and Y. Tan, *Nature Communications*, 2019, **10**, 1743.
144. J. Liu, M. Jiao, L. Lu, H. M. Barkholtz, Y. Li, Y. Wang, L. Jiang, Z. Wu, D.-j. Liu, L. Zhuang, C. Ma, J. Zeng, B. Zhang, D. Su, P. Song, W. Xing, W. Xu, Y. Wang, Z. Jiang and G. Sun, *Nature Communications*, 2017, **8**, 15938.
145. X. X. Wang, D. A. Cullen, Y.-T. Pan, S. Hwang, M. Wang, Z. Feng, J. Wang, M. H. Engelhard, H. Zhang, Y. He, Y. Shao, D. Su, K. L. More, J. S. Spendelow and G. Wu, *Advanced Materials*, 2018, **30**, 1706758.
146. C. Zhu, S. Fu, J. Song, Q. Shi, D. Su, M. H. Engelhard, X. Li, D. Xiao, D. Li, L. Estevez, D. Du and Y. Lin, *Small*, 2017, **13**, 1603407.
147. M. Naguib, M. Kurtoglu, V. Presser, J. Lu, J. Niu, M. Heon, L. Hultman, Y. Gogotsi and M. W. Barsoum, *Advanced Materials*, 2011, **23**, 4248-4253.
148. T. Y. Ma, J. L. Cao, M. Jaroniec and S. Z. Qiao, *Angewandte Chemie International Edition*, 2016, **55**, 1138-1142.
149. Q. Xue, Z. Pei, Y. Huang, M. Zhu, Z. Tang, H. Li, Y. Huang, N. Li, H. Zhang and C. Zhi, *Journal of Materials Chemistry A*, 2017, **5**, 20818-20823.
150. D. A. Kuznetsov, Z. Chen, P. V. Kumar, A. Tsoukalou, A. Kierzkowska, P. M. Abdala, O. V. Safonova, A. Fedorov and C. R. Müller, *Journal of the American Chemical Society*, 2019, **141**, 17809-17816.
151. J. Zhang, Y. Zhao, X. Guo, C. Chen, C.-L. Dong, R.-S. Liu, C.-P. Han, Y. Li, Y. Gogotsi and G. Wang, *Nature Catalysis*, 2018, **1**, 985-992.
152. A. D. Handoko, K. D. Fredrickson, B. Anasori, K. W. Convey, L. R. Johnson, Y. Gogotsi, A. Vojvodic and Z. W. Seh, *ACS Applied Energy Materials*, 2018, **1**, 173-180.
153. P. Li, J. Zhu, A. D. Handoko, R. Zhang, H. Wang, D. Legut, X. Wen, Z. Fu, Z. W. Seh and Q. Zhang, *Journal of Materials Chemistry A*, 2018, **6**, 4271-4278.

154. A. D. Handoko, S. N. Steinmann and Z. W. Seh, *Nanoscale Horizons*, 2019, **4**, 809-827.
155. J. Di, C. Yan, A. D. Handoko, Z. W. Seh, H. Li and Z. Liu, *Materials Today*, 2018, **21**, 749-770.
156. M. Gong, W. Zhou, M.-C. Tsai, J. Zhou, M. Guan, M.-C. Lin, B. Zhang, Y. Hu, D.-Y. Wang, J. Yang, S. J. Pennycook, B.-J. Hwang and H. Dai, *Nature Communications*, 2014, **5**, 4695.
157. T. Zhang, M.-Y. Wu, D.-Y. Yan, J. Mao, H. Liu, W.-B. Hu, X.-W. Du, T. Ling and S.-Z. Qiao, *Nano Energy*, 2018, **43**, 103-109.
158. X. Yan, L. Tian and X. Chen, *Journal of Power Sources*, 2015, **300**, 336-343.
159. T. Ling, T. Zhang, B. Ge, L. Han, L. Zheng, F. Lin, Z. Xu, W.-B. Hu, X.-W. Du, K. Davey and S.-Z. Qiao, *Advanced Materials*, 2019, **31**, 1807771.
160. J. Wang, S. Mao, Z. Liu, Z. Wei, H. Wang, Y. Chen and Y. Wang, *ACS Applied Materials & Interfaces*, 2017, **9**, 7139-7147.
161. L.-L. Feng, G. Yu, Y. Wu, G.-D. Li, H. Li, Y. Sun, T. Asefa, W. Chen and X. Zou, *Journal of the American Chemical Society*, 2015, **137**, 14023-14026.
162. N. Jiang, Q. Tang, M. Sheng, B. You, D.-e. Jiang and Y. Sun, *Catalysis Science & Technology*, 2016, **6**, 1077-1084.
163. A. Sivanantham, P. Ganesan and S. Shanmugam, *Advanced Functional Materials*, 2016, **26**, 4661-4672.
164. J. Li, P. K. Shen and Z. Tian, *International Journal of Hydrogen Energy*, 2017, **42**, 7136-7142.
165. M. Yang, Y. Jiang, S. Liu, M. Zhang, Q. Guo, W. Shen, R. He, W. Su and M. Li, *Nanoscale*, 2019, **11**, 14016-14023.
166. Y. Xie, Y. Liu and Z. Yang, *International Journal of Hydrogen Energy*, 2020, **45**, 6500-6507.
167. Y. Xia, W. Wu, H. Wang, S. Rao, F. Zhang and G. Zou, *Nanotechnology*, 2020, **31**, 145401.
168. Y. Wan, Z. Zhang, X. Xu, Z. Zhang, P. Li, X. Fang, K. Zhang, K. Yuan, K. Liu, G. Ran, Y. Li, Y. Ye and L. Dai, *Nano Energy*, 2018, **51**, 786-792.
169. J. Hu, B. Huang, C. Zhang, Z. Wang, Y. An, D. Zhou, H. Lin, M. K. H. Leung and S. Yang, *Energy & Environmental Science*, 2017, **10**, 593-603.
170. Y. Tan, P. Liu, L. Chen, W. Cong, Y. Ito, J. Han, X. Guo, Z. Tang, T. Fujita, A. Hirata and M. W. Chen, *Advanced Materials*, 2014, **26**, 8023-8028.
171. Q. Xu, Y. Liu, H. Jiang, Y. Hu, H. Liu and C. Li, *Advanced Energy Materials*, 2019, **9**, 1970004.
172. Y. Yin, J. Han, Y. Zhang, X. Zhang, P. Xu, Q. Yuan, L. Samad, X. Wang, Y. Wang, Z. Zhang, P. Zhang, X. Cao, B. Song and S. Jin, *Journal of the American Chemical Society*, 2016, **138**, 7965-7972.
173. P. Liu, J. Zhu, J. Zhang, P. Xi, K. Tao, D. Gao and D. Xue, *ACS Energy Letters*, 2017, **2**, 745-752.
174. H. Li, S. Chen, X. Jia, B. Xu, H. Lin, H. Yang, L. Song and X. Wang, *Nature Communications*, 2017, **8**, 15377.
175. Y. Yin, Y. Zhang, T. Gao, T. Yao, X. Zhang, J. Han, X. Wang, Z. Zhang, P. Xu, P. Zhang, X. Cao, B. Song and S. Jin, *Advanced Materials*, 2017, **29**, 1700311.

176. L. Najafi, S. Bellani, R. Oropesa-Nuñez, A. Ansaldo, M. Prato, A. E. Del Rio Castillo and F. Bonaccorso, *Advanced Energy Materials*, 2018, **8**, 1703212.
177. D. Gao, B. Xia, C. Zhu, Y. Du, P. Xi, D. Xue, J. Ding and J. Wang, *Journal of Materials Chemistry A*, 2018, **6**, 510-515.
178. C. Tan, Z. Luo, A. Chaturvedi, Y. Cai, Y. Du, Y. Gong, Y. Huang, Z. Lai, X. Zhang, L. Zheng, X. Qi, M. H. Goh, J. Wang, S. Han, X.-J. Wu, L. Gu, C. Kloc and H. Zhang, *Advanced Materials*, 2018, **30**, 1705509.
179. M. A. Lukowski, A. S. Daniel, C. R. English, F. Meng, A. Forticaux, R. J. Hamers and S. Jin, *Energy & Environmental Science*, 2014, **7**, 2608-2613.
180. X. Shi, M. Fields, J. Park, J. M. McEnaney, H. Yan, Y. Zhang, C. Tsai, T. F. Jaramillo, R. Sinclair, J. K. Nørskov and X. Zheng, *Energy & Environmental Science*, 2018, **11**, 2270-2277.
181. Y. Chen, S. Xu, Y. Li, R. J. Jacob, Y. Kuang, B. Liu, Y. Wang, G. Pastel, L. G. Salamanca-Riba, M. R. Zachariah and L. Hu, *Advanced Energy Materials*, 2017, **7**, 1700482.
182. V.-T. Nguyen, P. A. Le, Y.-C. Hsu and K.-H. Wei, *ACS Applied Materials & Interfaces*, 2020, **12**, 11533-11542.
183. Y. Yang, K. Zhang, H. Lin, X. Li, H. C. Chan, L. Yang and Q. Gao, *ACS Catalysis*, 2017, **7**, 2357-2366.
184. J. Miao, F.-X. Xiao, H. B. Yang, S. Y. Khoo, J. Chen, Z. Fan, Y.-Y. Hsu, H. M. Chen, H. Zhang and B. Liu, *Science Advances*, 2015, **1**, e1500259.
185. S. Piontek, C. Andronescu, A. Zaichenko, B. Konkena, K. junge Puring, B. Marler, H. Antoni, I. Sinev, M. Muhler, D. Mollenhauer, B. Roldan Cuenya, W. Schuhmann and U.-P. Apfel, *ACS Catalysis*, 2018, **8**, 987-996.
186. J. Yu, W.-J. Li, H. Zhang, F. Zhou, R. Li, C.-Y. Xu, L. Zhou, H. Zhong and J. Wang, *Nano Energy*, 2019, **57**, 222-229.
187. Y. Ito, W. Cong, T. Fujita, Z. Tang and M. Chen, *Angewandte Chemie International Edition*, 2015, **54**, 2131-2136.
188. T. Li, D. Tang, Z. Cui, B. Cai, D. Li, Q. Chen and C. Li, *Electrocatalysis*, 2018, **9**, 573-581.
189. K. Qu, Y. Zheng, Y. Jiao, X. Zhang, S. Dai and S.-Z. Qiao, *Advanced Energy Materials*, 2017, **7**, 1602068.
190. J. Zhang, L. Qu, G. Shi, J. Liu, J. Chen and L. Dai, *Angewandte Chemie International Edition*, 2016, **55**, 2230-2234.
191. Y. Zhao, F. Zhao, X. Wang, C. Xu, Z. Zhang, G. Shi and L. Qu, *Angewandte Chemie International Edition*, 2014, **53**, 13934-13939.
192. M. Tavakkoli, N. Holmberg, R. Kronberg, H. Jiang, J. Sainio, E. I. Kauppinen, T. Kallio and K. Laasonen, *ACS Catalysis*, 2017, **7**, 3121-3130.
193. L. Zhang, L. Han, H. Liu, X. Liu and J. Luo, *Angewandte Chemie International Edition*, 2017, **56**, 13694-13698.
194. Y. Qu, B. Chen, Z. Li, X. Duan, L. Wang, Y. Lin, T. Yuan, F. Zhou, Y. Hu, Z. Yang, C. Zhao, J. Wang, C. Zhao, Y. Hu, G. Wu, Q. Zhang, Q. Xu, B. Liu, P. Gao, R. You, W. Huang, L. Zheng, L. Gu, Y. Wu and Y. Li, *Journal of the American Chemical Society*, 2019, **141**, 4505-4509.
195. H. Zhang, P. An, W. Zhou, B. Y. Guan, P. Zhang, J. Dong and X. W. Lou, *Science Advances*, 2018, **4**, eaao6657.

196. W. Liu, Q. Xu, P. Yan, J. Chen, Y. Du, S. Chu and J. Wang, *ChemCatChem*, 2018, **10**, 946-950.
197. S. Ye, F. Luo, Q. Zhang, P. Zhang, T. Xu, Q. Wang, D. He, L. Guo, Y. Zhang, C. He, X. Ouyang, M. Gu, J. Liu and X. Sun, *Energy & Environmental Science*, 2019, **12**, 1000-1007.
198. M. Li, K. Duanmu, C. Wan, T. Cheng, L. Zhang, S. Dai, W. Chen, Z. Zhao, P. Li, H. Fei, Y. Zhu, R. Yu, J. Luo, K. Zang, Z. Lin, M. Ding, J. Huang, H. Sun, J. Guo, X. Pan, W. A. Goddard, P. Sautet, Y. Huang and X. Duan, *Nature Catalysis*, 2019, **2**, 495-503.
199. Z. Luo, Y. Ouyang, H. Zhang, M. Xiao, J. Ge, Z. Jiang, J. Wang, D. Tang, X. Cao, C. Liu and W. Xing, *Nature Communications*, 2018, **9**, 2120.
200. T. Chao, X. Luo, W. Chen, B. Jiang, J. Ge, Y. Lin, G. Wu, X. Wang, Y. Hu, Z. Zhuang, Y. Wu, X. Hong and Y. Li, *Angewandte Chemie International Edition*, 2017, **56**, 16047-16051.
201. J. Yang, B. Chen, X. Liu, W. Liu, Z. Li, J. Dong, W. Chen, W. Yan, T. Yao, X. Duan, Y. Wu and Y. Li, *Angewandte Chemie International Edition*, 2018, **57**, 9495-9500.
202. S. Yuan, Z. Pu, H. Zhou, J. Yu, I. S. Amiinu, J. Zhu, Q. Liang, J. Yang, D. He, Z. Hu, G. Van Tendeloo and S. Mu, *Nano Energy*, 2019, **59**, 472-480.
203. L. Zhang, R. Si, H. Liu, N. Chen, Q. Wang, K. Adair, Z. Wang, J. Chen, Z. Song, J. Li, M. N. Banis, R. Li, T.-K. Sham, M. Gu, L.-M. Liu, G. A. Botton and X. Sun, *Nature Communications*, 2019, **10**, 4936.
204. Y. Xue, B. Huang, Y. Yi, Y. Guo, Z. Zuo, Y. Li, Z. Jia, H. Liu and Y. Li, *Nature Communications*, 2018, **9**, 1460.
205. L. Fan, P. F. Liu, X. Yan, L. Gu, Z. Z. Yang, H. G. Yang, S. Qiu and X. Yao, *Nature Communications*, 2016, **7**, 10667.
206. H. Fei, J. Dong, M. J. Arellano-Jiménez, G. Ye, N. Dong Kim, E. L. G. Samuel, Z. Peng, Z. Zhu, F. Qin, J. Bao, M. J. Yacaman, P. M. Ajayan, D. Chen and J. M. Tour, *Nature Communications*, 2015, **6**, 8668.
207. L. Cao, Q. Luo, W. Liu, Y. Lin, X. Liu, Y. Cao, W. Zhang, Y. Wu, J. Yang, T. Yao and S. Wei, *Nature Catalysis*, 2019, **2**, 134-141.
208. J.-D. Yi, R. Xu, G.-L. Chai, T. Zhang, K. Zang, B. Nan, H. Lin, Y.-L. Liang, J. Lv, J. Luo, R. Si, Y.-B. Huang and R. Cao, *Journal of Materials Chemistry A*, 2019, **7**, 1252-1259.
209. W. Chen, J. Pei, C.-T. He, J. Wan, H. Ren, Y. Zhu, Y. Wang, J. Dong, S. Tian, W.-C. Cheong, S. Lu, L. Zheng, X. Zheng, W. Yan, Z. Zhuang, C. Chen, Q. Peng, D. Wang and Y. Li, *Angewandte Chemie International Edition*, 2017, **56**, 16086-16090.
210. W. Chen, J. Pei, C.-T. He, J. Wan, H. Ren, Y. Wang, J. Dong, K. Wu, W.-C. Cheong, J. Mao, X. Zheng, W. Yan, Z. Zhuang, C. Chen, Q. Peng, D. Wang and Y. Li, *Advanced Materials*, 2018, **30**, 1800396.
211. S. Li, P. Tuo, J. Xie, X. Zhang, J. Xu, J. Bao, B. Pan and Y. Xie, *Nano Energy*, 2018, **47**, 512-518.
212. Y. Jiang, T. Sun, X. Xie, W. Jiang, J. Li, B. Tian and C. Su, *ChemSusChem*, 2019, **12**, 1368-1373.
213. Y. Yoon, A. P. Tiwari, M. Lee, M. Choi, W. Song, J. Im, T. Zyung, H.-K. Jung, S. S. Lee, S. Jeon and K.-S. An, *Journal of Materials Chemistry A*, 2018, **6**, 20869-20877.

214. W. Yuan, L. Cheng, Y. An, H. Wu, N. Yao, X. Fan and X. Guo, *ACS Sustainable Chemistry & Engineering*, 2018, **6**, 8976-8982.
215. C.-F. Du, X. Sun, H. Yu, Q. Liang, K. N. Dinh, Y. Zheng, Y. Luo, Z. Wang and Q. Yan, *Advanced Science*, 2019, **6**, 1900116.
216. Z. Li, Z. Qi, S. Wang, T. Ma, L. Zhou, Z. Wu, X. Luan, F.-Y. Lin, M. Chen, J. T. Miller, H. Xin, W. Huang and Y. Wu, *Nano Letters*, 2019, **19**, 5102-5108.
217. Y. Yuan, H. Li, L. Wang, L. Zhang, D. Shi, Y. Hong and J. Sun, *ACS Sustainable Chemistry & Engineering*, 2019, **7**, 4266-4273.
218. J. Liang, C. Ding, J. Liu, T. Chen, W. Peng, Y. Li, F. Zhang and X. Fan, *Nanoscale*, 2019, **11**, 10992-11000.
219. N. H. Attanayake, S. C. Abeyweera, A. C. Thenuwara, B. Anasori, Y. Gogotsi, Y. Sun and D. R. Strongin, *Journal of Materials Chemistry A*, 2018, **6**, 16882-16889.
220. C.-F. Du, K. N. Dinh, Q. Liang, Y. Zheng, Y. Luo, J. Zhang and Q. Yan, *Advanced Energy Materials*, 2018, **8**, 1801127.
221. X. Wu, Z. Wang, M. Yu, L. Xiu and J. Qiu, *Advanced Materials*, 2017, **29**, 1607017.
222. L. Xiu, Z. Wang, M. Yu, X. Wu and J. Qiu, *ACS Nano*, 2018, **12**, 8017-8028.
223. P. Charoen-amornkitt, T. Suzuki and S. Tsushima, *Electrochimica Acta*, 2017, **258**, 433-441.
224. J. Scholz, M. Risch, K. A. Stoerzinger, G. Wartner, Y. Shao-Horn and C. Jooss, *The Journal of Physical Chemistry C*, 2016, **120**, 27746-27756.
225. C. C. L. McCrory, S. Jung, J. C. Peters and T. F. Jaramillo, *Journal of the American Chemical Society*, 2013, **135**, 16977-16987.
226. Y. Yoon, B. Yan and Y. Surendranath, *Journal of the American Chemical Society*, 2018, **140**, 2397-2400.
227. S. Jung, C. C. L. McCrory, I. M. Ferrer, J. C. Peters and T. F. Jaramillo, *Journal of Materials Chemistry A*, 2016, **4**, 3068-3076.
228. B. M. Weckhuysen, *Phys. Chem. Chem. Phys.*, 2003, **5**, 4351-4360.
229. M. A. Bañares, *Catalysis Today*, 2005, **100**, 71-77.
230. C. Hu, Q. Ma, S.-F. Hung, Z.-N. Chen, D. Ou, B. Ren, H. M. Chen, G. Fu and N. Zheng, *Chem*, 2017, **3**, 122-133.
231. N. Kornienko, J. Resasco, N. Becknell, C.-M. Jiang, Y.-S. Liu, K. Nie, X. Sun, J. Guo, S. R. Leone and P. Yang, *Journal of the American Chemical Society*, 2015, **137**, 7448-7455.
232. H. G. S. Casalongue, J. D. Benck, C. Tsai, R. K. B. Karlsson, S. Kaya, M. L. Ng, L. G. M. Pettersson, F. Abild-Pedersen, J. K. Nørskov, H. Ogasawara, T. F. Jaramillo and A. Nilsson, *The Journal of Physical Chemistry C*, 2014, **118**, 29252-29259.
233. J. H. K. Pfisterer, Y. Liang, O. Schneider and A. S. Bandarenka, *Nature*, 2017, **549**, 74-77.
234. A. J. R. Hensley, K. Ghale, C. Rieg, T. Dang, E. Anderst, F. Studt, C. T. Campbell, J.-S. McEwen and Y. Xu, *The Journal of Physical Chemistry C*, 2017, **121**, 4937-4945.
235. Y. Ihm, C. Park, J. Jakowski, J. R. Morris, J. H. Shim, Y.-H. Kim, B. G. Sumpter and M. Yoon, *The Journal of Physical Chemistry C*, 2018, **122**, 26189-26195.
236. C. J. Cramer and D. G. Truhlar, *Journal of the American Chemical Society*, 1991, **113**, 8305-8311.

237. J. Sun, A. Ruzsinszky and J. P. Perdew, *Physical Review Letters*, 2015, **115**, 036402.
238. Y. Zhao, N. González-García and D. G. Truhlar, *The Journal of Physical Chemistry A*, 2005, **109**, 2012-2018.
239. N. L. Nguyen, N. Colonna, A. Ferretti and N. Marzari, *Physical Review X*, 2018, **8**, 021051.
240. J. Ma and L.-W. Wang, *Scientific Reports*, 2016, **6**, 24924.
241. T. J. Smart, F. Wu, M. Govoni and Y. Ping, *Physical Review Materials*, 2018, **2**, 124002.
242. G. Miceli, W. Chen, I. Reshetnyak and A. Pasquarello, *Physical Review B*, 2018, **97**, 121112.
243. N. P. Brawand, M. Govoni, M. Vörös and G. Galli, *Journal of Chemical Theory and Computation*, 2017, **13**, 3318-3325.
244. H. Zheng, M. Govoni and G. Galli, *Physical Review Materials*, 2019, **3**, 073803.
245. W. Chen, G. Miceli, G.-M. Rignanese and A. Pasquarello, *Physical Review Materials*, 2018, **2**, 073803.
246. P. Liu, C. Franchini, M. Marsman and G. Kresse, *Journal of Physics: Condensed Matter*, 2019, **32**, 015502.
247. P. S. Schmidt and K. S. Thygesen, *The Journal of Physical Chemistry C*, 2018, **122**, 4381-4390.
248. C. A. Gaggioli, S. J. Stoneburner, C. J. Cramer and L. Gagliardi, *ACS Catalysis*, 2019, **9**, 8481-8502.
249. T. Bligaard, R. M. Bullock, C. T. Campbell, J. G. Chen, B. C. Gates, R. J. Gorte, C. W. Jones, W. D. Jones, J. R. Kitchin and S. L. Scott, *ACS Catalysis*, 2016, **6**, 2590-2602.
250. W. B. Schneider and A. A. Auer, *Beilstein Journal of Nanotechnology*, 2014, **5**, 668-676.
251. Z. Wang, Y. Yang, D. L. Olmsted, M. Asta and B. B. Laird, *The Journal of Chemical Physics*, 2014, **141**, 184102.
252. R. E. Skyner, J. L. McDonagh, C. R. Groom, T. van Mourik and J. B. O. Mitchell, *Physical Chemistry Chemical Physics*, 2015, **17**, 6174-6191.
253. J. Zhang, H. Zhang, T. Wu, Q. Wang and D. van der Spoel, *Journal of Chemical Theory and Computation*, 2017, **13**, 1034-1043.
254. K. Mathew, R. Sundararaman, K. Letchworth-Weaver, T. A. Arias and R. G. Hennig, *The Journal of Chemical Physics*, 2014, **140**, 084106.
255. C. J. Cramer and D. G. Truhlar, *Chemical Reviews*, 1999, **99**, 2161-2200.
256. A. V. Marenich, R. M. Olson, C. P. Kelly, C. J. Cramer and D. G. Truhlar, *Journal of Chemical Theory and Computation*, 2007, **3**, 2011-2033.
257. A. Fortunelli and J. Tomasi, *Chemical Physics Letters*, 1994, **231**, 34-39.
258. O. Andreussi, I. Dabo and N. Marzari, *The Journal of Chemical Physics*, 2012, **136**, 064102.
259. C. Dupont, O. Andreussi and N. Marzari, *The Journal of Chemical Physics*, 2013, **139**, 214110.
260. T. Shinagawa and K. Takanabe, *Journal of Power Sources*, 2015, **287**, 465-471.
261. Y. Ping, R. Sundararaman and W. A. Goddard Iii, *Physical Chemistry Chemical Physics*, 2015, **17**, 30499-30509.

262. K. Schwarz, B. Xu, Y. Yan and R. Sundararaman, *Physical Chemistry Chemical Physics*, 2016, **18**, 16216-16223.
263. M. A. Butler, R. D. Nasby and R. K. Quinn, *Solid State Communications*, 1976, **19**, 1011-1014.

ToC figure

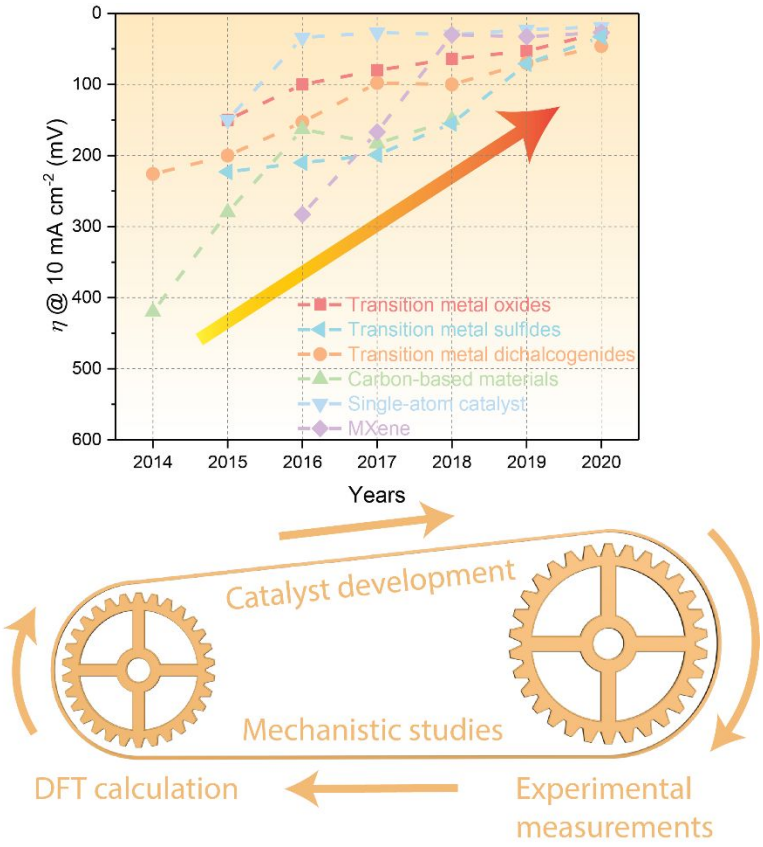
0
100
200
300
400
500
600
η @ 10 mA cm-2 (mV)
2014
2015
2016
2017
2018
2019
2020
Years
Transition metal oxides
Transition metal sulfides
Transition metal dichalcogenides
Carbon-based materials
Single-atom catalyst
MXene
Catalyst development
Mechanistic studies
DFT calculation
Experimental measurements